Eastern Bering Sea shelf environmental and lower trophic level responses to climate forcing: Results of dynamical downscaling from CMIP6

Wei Cheng [a,b,*], Albert J. Hermann [a,b], Anne B. Hollowed [c], Kirstin K. Holsman [c], Kelly A. Kearney [a,c], Darren J. Pilcher [a,b], Charles A. Stock [d], Kerim Y. Aydin [c]

[a] University of Washington, Cooperative Institute for Climate, Ocean and Ecosystem Studies, Seattle, WA, USA
[b] NOAA, Pacific Marine Environmental Laboratory, Seattle, WA, USA
[c] NOAA, Alaska Fisheries Science Center, Seattle, WA, USA
[d] NOAA, Geophysical Fluid Dynamics Laboratory, Princeton, NJ, USA

ARTICLE INFO

ABSTRACT

In this study we present projected changes in the Eastern Bering Sea shelf (EBS) biophysical processes in response to climate forcing scenarios from the Coupled Model Intercomparison Phase 6 (CMIP6). These changes are obtained by dynamical downscaling using a Bering Sea regional model. Surface atmospheric and ocean boundary forcing from three Earth System Models (ESMs) in CMIP6, and a low and a high emission scenario of Shared Socioeconomic Pathway (SSP126 and SSP585) of each of the ESMs are considered. Ensemble mean results suggest that, contrary to an anticipated increase in ocean stratification under warming, diminishing ice cover in response to climate forcing and resultant reduced surface freshening *weakens* EBS stratification in the melt season. Modeled ensemble mean phytoplankton and zooplankton biomass on the EBS exhibits subsurface maxima during the growing season; the amplitude of these maxima decreases with warming, along with a reduction in primary productivity and oxygen concentration over much of the EBS water column. Phenology of both phytoplankton and zooplankton biomass on the EBS shifts earlier, leading to an increase (decrease) in biomass averaged between April–July (August–November), while annually averaged biomass decreases under warming. Projected changes of primary and secondary plankton biomass at the end of the 21st century are not well separated between the SSP126 and SSP585 scenario in light of the large across model spread under each scenario. The projected ensemble mean warming amplitude of the EBS summer bottom temperature is largely unchanged between results forced by the Coupled Model Intercomparison Phase 5 Representative Concentration Pathway 8.5 (CMIP5 RCP8.5) and CMIP6 SSP585 scenarios. Likewise, the reduction rate of annual mean phytoplankton and large zooplankton biomass are comparable between RCP8.5 and SSP585 projections, even though the absolute amplitudes of biomass are sensitive to modeling parameters such as the solar irradiance attenuation curve. Hence, within the Bering Sea dynamical downscaling framework, projected long-term warming trends in EBS bottom temperature and plankton biomass reduction rates are robust responses to climate forcing.

1. Introduction

In the last decade, numerous coupled model interdisciplinary research teams have endeavored to project the implications of climate change on marine ecosystems (Tittensor et al., 2018; Bryndum-Buchholz et al., 2019; Payne et al., 2020). These efforts have contrasted climate futures under alternative emission scenarios (O'Neill et al., 2014), fishing scenarios (Groeneveld et al., 2018), and in some cases alternative ecosystem model structures (Cheung et al., 2019). The Alaska Climate Integrated Modeling (ACLIM) project utilizes dynamic climate model downscaling to project impacts on marine ecosystems in the eastern Bering Sea and the implications of these changes for communities dependent on the region's living marine resources (Hollowed et al., 2020). The ACLIM project employs a multi-model approach to assess the contributions of model complexity, emission scenario uncertainty, and global Earth System Model (ESM) structural differences on the projected

---

impacts of climate change on the eastern Bering Sea shelf (hereafter, referred to as EBS) ecosystem under current and alternative management scenarios (Hollowed et al., 2020).

The EBS subarctic marine ecosystem has undergone rapid physical changes in the last decade in response to shifting climate conditions (Stabeno et al., 2017; Stabeno and Bell, 2019). These changes have triggered complex ecological adjustments across trophic levels such as delayed spring bloom in anomalously warm years, low abundances of large crustacean zooplankton, and seabird die-offs (Sigler et al., 2010; Duffy-Anderson et al., 2019; Stevenson and Lauth, 2019; Siddon et al., 2020), and some of these changes have important implications for the future of commercial fisheries in the region (Eisner et al., 2020; Holsman et al., 2020; Reum et al., 2020). In ACLIM phase I, a regional ocean model with 10 km grid spacing (hereafter referred to as the Bering10K model) was coupled to a biogeochemical model (Gibson and Spitz, 2011) to project future marine ecosystem states of the region under different future emission scenarios. The Bering10K modeling system was developed to resolve relevant physical and biogeochemical processes impacted by climate at the appropriate spatial and temporal resolution (Hermann et al., 2013). Earlier versions of Bering10K have been used in dynamical downscaling of EBS for the past decades (Ortiz et al., 2016) and for climate change projections (Hermann et al., 2013, 2016).

Since then, the Bering10K model has undergone further improvements (detailed in Section 2) and reached a mature phase in 2017, allowing the ACLIM research team to propose testing the operational capability of the existing coupled model enterprise. Here, the term "operational" is used in the sense that the team could rapidly update regional downscaling software (originally built for the existing coupled model) upon receipt of results from the Coupled Model Intercomparison Project (CMIP) phase 6 (CMIP6) (Eyring et al., 2016) under different scenarios (O'Neill et al., 2016). CMIP is a coordinated model inter-comparison project where the world's climate research centers carry out global Earth System Model (ESM) simulations under the same Greenhouse Gases (GHGs) and aerosol emission scenarios and the simulations are cross compared and used to assess climate change uncertainties. Phases of CMIP occur roughly every five years along with the updates of GHGs and aerosol forcing scenarios, and currently CMIP is in its 6th phase. Long simulations (from multi-centennial to multi-millennial time scales) of the global ESMs necessitate the use of coarse horizontal resolutions (nominally 1° longitude/latitude mesh size in the ocean). However, these coarse-resolution global simulations fail to capture biophysical features that play a key role in mediating upper trophic level responses to climate change. For example, in the EBS region, the global models fail to capture critical spatial and temporal variations of the "cold pool" (bottom waters on the ESB with temperature colder than 2°C), cross-shelf variations in seasonal stratification, and other fine-scale circulation features that influence the growth and survival of many fisheries species (Hermann et al., 2016; Kearney et al., 2020). Dynamical downscaling, i.e. running a finer-resolution regional ocean model driven by air-sea fluxes and lateral boundary conditions derived from a larger domain, coarser-resolution model, can help resolve these important features. Besides providing information on fine spatial scales, operationalizing the Bering10K model extends the ACLIM project assessment of uncertainty by measuring the contribution of structural changes across global ESM phases, and improvements to the Bering10K biogeochemical model itself (Pilcher et al., 2019; Kearney et al., 2020), to changes in future regional projections. To our knowledge, this type of evaluation of the respective roles of structural changes to ESMs and improvements to a regional ocean circulation model with biogeochemistry on downscaled future ocean projections has not been attempted using a coupled regional biophysical modeling framework.

Operationalizing the Bering10K model also enables a timely dissemination of scale-relevant climate information for future climate impact assessments. The Intergovernmental Panel on Climate Change (IPCC) guidelines for assessment report authors encourage reliance on findings published in the peer reviewed literature (Mastrandrea et al.,

2011). The short time period between the release of updated global ESM model projections and the due dates for submission of the IPCC assessment reports has previously precluded the ability to complete processing and publication of updated downscaled high resolution ocean model results necessary for ecosystem change assessment. The state-of-the-art has matured to a point where updates of the Bering10K modeling enterprise can occur rapidly, providing regional projections of future ecosystem states in time for consideration by IPCC assessment teams. This would allow key findings identified by working group I of the IPCC to be fully considered by authors of working groups II and III.

Under this background, we have recently completed a Bering Sea dynamical downscaling suite driven by selected CMIP6 models. In this study, we perform a baseline assessment of key biophysical changes in the EBS Large Marine Ecosystem (LME) in response to climate forcing from these new simulations, and compare results with previous downscaled simulations forced by the ESMs from CMIP phase 5 (CMIP5), the previous phase of CMIP. In particular, we focus on spatiotemporal characteristics of the environmental and lower trophic level responses critical to early life history and fish larvae survival (Aydin and Mueter, 2007; Duffy-Anderson et al., 2016) but these have not been analyzed in great detail in previous investigations. These characteristics include phytoplankton and zooplankton seasonal bloom timing and plankton biomass adjustment trends specific to each EBS biophysical domain. We also examine vertical distribution of phytoplankton biomass on EBS, information not readily available from satellite remote sensing and coarse resolution global ESMs. We examine mainly individual biophysical processes but links between the variables are noted where applicable. Formal quantification of co-variability between the variables using multivariate EOF analyses are presented in a companion paper (Hermann et al., 2021, this issue), where identified co-variability is also used to expand the regional downscaling ensemble size.

The rest of the paper is organized as follows. In Section 2, we introduce the three CMIP6 global ESMs selected and the reasons behind those selections, followed by a summary on the Bering10K biogeochemical model improvements and the diagnostic methods. The main results from this study are presented in Section 3. In Section 4 we discuss caveats and implications of the main results; the paper's conclusions appear in Section 5.

2. Methods

2.1. CMIP6 ESMs selection

To assess uncertainties, it is useful to downscale an ensemble of global ESMs, but the high computational and data management demands of the high-resolution Bering10K regional simulations limit the number of parent models that can be practically included in the ensemble.

Similar to previous studies (Hermann et al., 2016, 2019), our selection is based on three considerations: 1) regional characteristics of the Bering Sea; 2) amplitude of future warming; 3) continuity in the models used for CMIP5 and CMIP6 downscaling. The Eastern Bering Sea is seasonally covered by sea ice and there is strong interannual variability in the ice cover, and sea ice is a major driver of Bering Sea ecology (Sigler et al., 2010). Therefore, we first select global ESMs that capture the spatiotemporal characteristics of observed sea ice in the "historical" period (1980–2014) and eliminate those that perform poorly in this regard. Secondly, from the remaining models, we select ones that cover a range of possible future warmings (Drenkard et al., in press). Under a specific Green House Gas (GHG) and aerosol forcing scenario, differences in warming across the global ESMs are associated with their structural and parameter uncertainties. This step of selection was in part guided by published results on the equilibrium climate sensitivity (ECS) (Zelinka et al., 2020). ECS quantifies the equilibrium change in global-mean surface air temperature after a doubling of CO_2 concentration, and is a frequently used metric across ESMs. Lastly, from the

models that met criteria one and criteria two, to facilitate comparison of downscaled simulations across CMIP phases, we opted to use ESMs from the same modeling centers for both the CMIP5 and CMIP6 dynamical downscaling. Together, these considerations led us to choose the particular modeling centers and ESMs as summarized in Table 1.

The development of global ESMs is an ongoing process at each of the major climate modeling centers, and therefore the simulations submitted to each subsequent phase of the CMIP include the most recent upgrades to the atmosphere, ocean, land, sea ice, and ocean biogeochemistry components of each center's models. Between CMIP5 and CMIP6, the three models used in this study reflect the overall development trends across global ESMs toward improved resolution of smaller-scale ocean processes, increased comprehensiveness of biological components and their influence on the carbon cycle, and tighter coupling between land and ocean components (Séférian et al., 2020). Specifically, the GFDL-ESM4 model increased the vertical and horizontal resolution of its ocean module and migrated to a Z*-isopycnal hybrid coordinate system; within the biogeochemical module, it added explicit representation of zooplankton, refined the particle remineralization dynamics, and added additional nutrient exchanges between the ocean, atmosphere, and land (Stock et al., 2020; Dunne et al., 2020). Relative to its predecessor, MIROC-ES2L has increased resolution in their atmospheric model, and the ocean biogeochemistry module included the addition of diazotrophic phytoplankton, expanded links to the terrestrial nitrogen cycle, added oxygen cycling and denitrification processes, and introduced explicit tracking of the iron cycle (Hajima et al., 2020). Within its biogeochemical model, CESM2 improved sub-grid scale light processes, introduced variable C:P dynamics, added semi-labile and refractory organic material and a ligand tracer to complex with iron, and reconfigured burial processes to balance preindustrial river inputs (Danabasoglu et al., 2020).

As a result of these and other changes, the skill and climate sensitivity of the three models shifted between their CMIP5 and CMIP6 versions. The CESM2 model has improved historical simulations in comparison with the previous generation CESM1, and the ECS of CESM2 is significantly greater than that of CESM1 (Danabasoglu et al., 2020). MIROC-ES2L, on the other hand, saw a significant decrease in its ECS relative to its predecessor model, MIROC-ESM. The GFDL-ESM4 model maintained a comparable ECS to its predecessor, GFDL-ESM2, with both falling toward the lower end of the ECS range across both the CMIP5 and CMIP6 suite of models. Overall, CESM2 is among the CMIP6 models with relatively high ECS (>5°C) whereas both GFDL-ESM4 and MIROC have relatively low ECS (<3°C). Warming characteristics in the parent ESMs ultimately affect their regional downscaling, as will be shown in Section 3.

Anthropogenic forcing in CMIP5 is categorized by Representative Concentration Pathway (RCP) such as RCP8.5, where the number 8.5 denotes the atmospheric radiative forcing magnitude in W/m^2. In CMIP6, future climate forcing scenarios are called shared socioeconomic pathways (SSPs) such as SSP126, SSP585 and so on (O'Neill et al., 2016), where the first digit denotes the pathway number and the last two digits represent atmospheric radiation anomalies, so SSP585 corresponds to a global mean radiation anomaly at the tropopause of 8.5 W/m^2. CMIP5 RCP8.5 and CMIP6 SSP585 have quite similar net radiative forcing and global mean temperature increase in the 21st century

(Fig. 3 of O'Neill et al., 2016), both representing the high end of future pathways. For CMIP6 downscaling, we use the high- and low-end SSPs (i.e. SSP126 and SSP585) to capture a range of possible future states.

2.2. Bering10K

Bering10K physical model is implemented using the Regional Ocean Modeling System (ROMS), a terrain-following vertical coordinate general circulation model (Haidvogel et al., 2008). The ocean general circulation model with tidal mixing is coupled to a sea-ice module (Budgell, 2005) and ocean biogeochemistry component (Kearney et al., 2020). We used direct output of the global ESMs to drive the regional simulations for the entire period from 1980 to 2100. In general, no bias correction or modulation is applied to atmospheric and oceanic forcing variables except to the sea surface height from MIROC-ES2L and runoff (detailed below). Bering10K is forced at the sea surface through momentum and buoyancy flux exchange with the atmosphere via bulk aerodynamic formulae (Fairall et al., 1996), and CO_2 fluxes via air-sea gas exchange. The lateral boundaries of Bering10K are open and forced by a mixture of radiation and nudging boundary conditions (Marchesiello et al., 2001). The atmospheric forcing variables are daily time series of surface air temperature, surface specific humidity, surface wind vector, downward shortwave and longwave radiation fluxes at the sea surface, sea level pressure, precipitation, annual mean river runoff, and annual mean atmospheric CO_2 concentration. The ocean lateral boundary forcing variables are 3-D monthly ocean currents, potential temperature, salinity, and sea surface height for the physical component, and nitrate, ammonium, iron concentration, total alkalinity, oxygen, and dissolved inorganic carbon concentration for the biogeochemical component. Further details of the dynamical downscaling procedure are described in Hermann et al. (2021, this issue). MIROC-ES2L uses real freshwater flux at the sea surface and its ocean mass is not conserved. As a result, after several thousands of years of spin-up and pre-industrial control simulation, its global mean sea surface height is approximately 4 m. A 4-m constant is therefore removed from MIROC-ES2L SSH at every grid point throughout our integration. Special care was applied to runoff forcing because ESM projected runoffs do not capture the strong spatial gradient of runoff in the real world, therefore, we developed a monthly climatology from the interannual values of Kearney (2019), and for projected years, we modulated our runoff climatology with the ratio of future annual runoff to mean annual runoff over the "historical" period of each global model, where the spatial average is taken over the regional model domain (155°E-143°W and 44–71°N). Hence, for any future year, the calculated yearly runoff is a function of the projected yearly regional runoff, but the presently observed seasonality and spatial distribution is retained. The exact ensemble variant label and additional data references are provided in the supplementary material (Table S1).

The Bering10K lower trophic level components underwent coding and algorithm improvements as described in Kearney et al. (2020). The latest upgrade incorporates carbonate and oxygen dynamics (Pilcher et al., 2019). The primary changes between the Hermann et al. (2016) version of the BESTNPZ model and the Kearney et al. (2020) version include: 1) improved formulation for the role of chlorophyll, sediment, and organic matter on the attenuation of short wave radiation as

Table 1

Modeling Centers and global ESMs used in the CMIP6 and CMIP5 Bering Sea dynamical downscaling and their equilibrium climate sensitivity (ECS). ECS are obtained from Zelinka et al. (2020) where it is estimated using the Gregory method (Gregory et al., 2004).

Modeling Center	National Center For Atmospheric Research (NCAR)		NOAA Geophysical Fluid Dynamics Laboratory (GFDL)		Japan Agency for Marine-Earth Science and Technology (JAMSTEC)	
	CMIP5	CMIP6	CMIP5	CMIP6	CMIP5	CMIP6
Model Name	CESM1	CESM2-CAM6	GFDL-ESM2M	GFDL-ESM4	MIROC-ESM	MIROC-ES2L
ECS (°C)	2.94	5.15	2.44	2.7	4.65	2.66
model description	Kay et al. (2015)	Danabasoglu et al. (2020)	Dunne et al. (2012, 2013)	Dunne et al. (2020)	Watanabe et al. (2011)	Hajima et al. (2020)

available for phytoplankton photosynthesis and distribution of surface heat fluxes throughout the water column, 2) correction of non-mass-conservative behavior within the biological module, 3) removal of macronutrient nudging except at the lateral boundaries, and 4) adjustment of the euphausiid prey preferences to allow for detrital scavenging in winter; see Kearney et al. (2020) for further comparison of the two versions. In addition, vertical layers of the model have been increased from 10 used in Hermann et al. (2016, 2019) to 30 in the latest implementation, with stretched layer thickness - thinner in the upper water column and thicker at depth (a subset is shown in Fig. 1 b-c). Horizontal grid locations remain unchanged from its earlier version. The Bering10K hindcast simulation (1980–2018), forced by atmospheric and oceanic reanalysis products, was evaluated against observations and found to have high skills in replicating observed physical environment of the EBS including horizontal and vertical patterns of water movement, stratification, and temperature and salinity signatures of water masses on the shelf (Kearney et al., 2020). It is also able to capture the mean seasonal cycle of primary production in the EBS, even though its ability to reproduce observed interannual variability in nutrient cycling, primary production and zooplankton community composition remains limited (Kearney et al., 2020).

2.3. Diagnostic methods

Simulated EBS bottom temperature is compared with *in situ* measurements made by the NOAA Alaska Fisheries Science Center summer trawl survey since the 1970s. The survey starts from the southeast shelf and moves northward as the season progresses, and the survey window is centered around July but can span 2–3 months depending on the measurement schedule. Therefore the survey data are not strictly

synoptic but they nonetheless provide a valuable benchmark for model evaluation. To facilitate comparison with model simulations, we interpolate each year's survey data onto a regular 0.1° longitude by latitude grid and assume they are taken in July of each year, and this data set is used to ground truth model simulations.

Sea-ice concentration, the fraction of each ocean grid box occupied by sea ice, from the downscaled historical simulation (1980–2014) is evaluated against corresponding satellite observations. Monthly time series of satellite sea-ice concentration is available from the national snow and ice data center for the period of 1979 to the present, and we use its 1980–2014 data in our analysis to match with the modeled "historical" time period.

Original model output is saved as weekly averages from which we construct time series of monthly averages. All ensuing analyses are performed using the monthly time series. Monthly climatology of the downscaled projections is defined from three 35-year periods: 1980–2014 ("historical" climatology), 2031–2065 ("mid-century" climatology) and 2066–2100 ("late 21st century" climatology); the relatively long 35-year window was chosen to reduce potential biases caused by interannual to decadal variability when defining a climatology. Climate change signals are assessed by contrasting results from the latter two periods with those from the earlier period.

The Bering10K BGC model has two phytoplankton compartments (large and small phytoplankton, named PhL and PhS respectively). Whenever we use the term "phytoplankton" in the paper, it represents the sum of these two components unless otherwise noted. Zooplankton size classes, not counting the top predator "jellyfish", include six functional groups: microzooplankton (MZL), small-bodied copepods (Cop), shelf and oceanic euphausiids (EupS and EupO), shelf and oceanic large-bodied copepods (NCaS and NCaO). In our results, "large zooplankton"
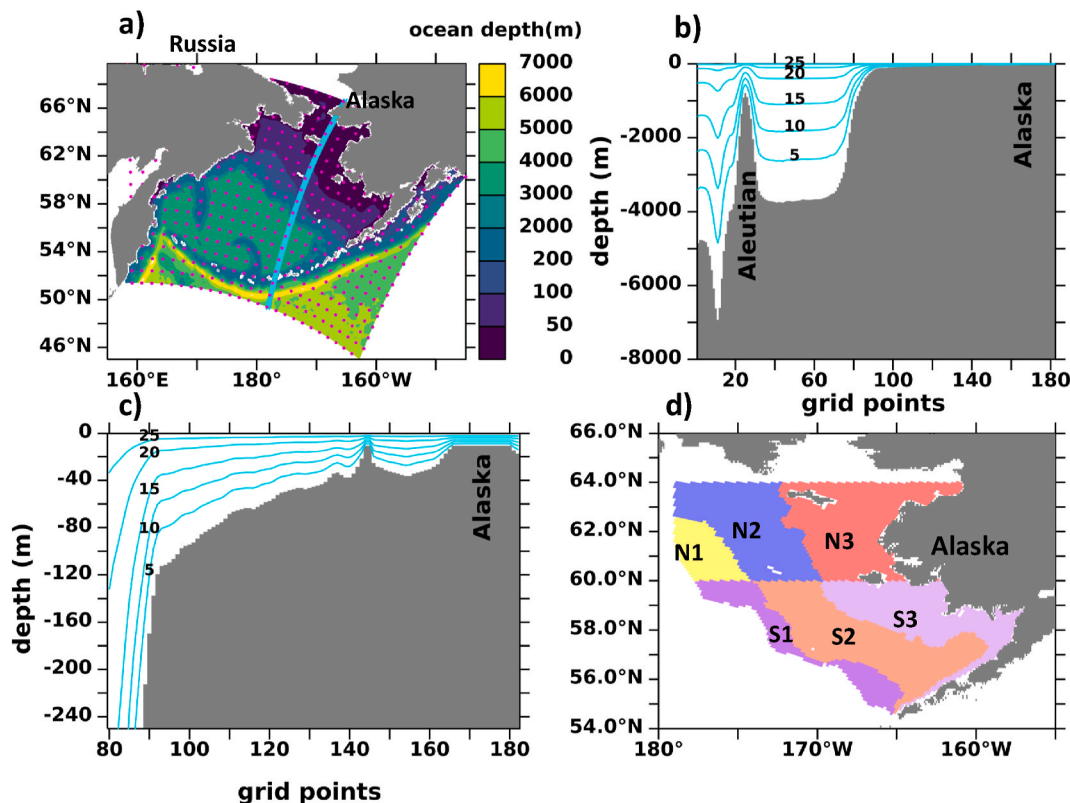

Fig. 1. ROMS Bering10K domain and horizontal grid points where one out of ten grid points in both coordinate directions are shown (a); terrain-following vertical coordinate layers along the cyan transect in a), for brevity, only K = 5, 10, 15, 20, 25 are shown (b); zoom-in of b) from surface to 250m and grid point 80 to 182 (c); Bering Sea shelf (depth ≤ 200m) bio-physical domains (d). Domains in d) are divided by the 50-m and 100-m isobaths in the cross-shelf direction and 60°N in the north-south direction. The domains north (south) of 60°N are named N1, N2 and N3 (S1, S2, and S3) respectively moving onshore, and these names are labeled in Figs. 11–13.

is the sum of Cop, EupS, EupO, NCaS, and NCaO. All lower trophic level biological state variables are expressed in the unit of mg C/m^3 using a constant nitrogen to carbon molar ratio of 16:106 (0.0126 mmol N (mg C)$^{-1}$). Additional detail regarding these state variables is available in Kearney et al. (2020).

We divide the year into three seasons: December-January-February-March (DJFM), April-May-June-July (AMJJ) and August-September-October-November (ASON) based on large zooplankton seasonal cycles, which corresponds to overwintering, spring growth, and fall decrease respectively. For consistency, we use the same time windows for phytoplankton seasonal aggregation but note that phytoplankton spring growth can be ahead of zooplankton growth. In our diagnosis, whenever horizontal spatial averaging is performed, it is weighted by the areas of each grid cell, and vertical averaging is weighted by layer thickness. No vertical interpolation to constant depths is attempted, so vertical distribution of fields are displayed either as a function of native vertical coordinate layers, where K = 30 (K = 1) corresponds to sea surface (ocean bottom), or *mean depth* of the vertical layer averaged over the corresponding horizontal domain.

To examine spatial heterogeneity, our analysis uses the historical division of the EBS (Coachman, 1986) and addresses each subdomain (colored areas in Fig. 1d) specifically: 0–50 m is the inner shelf domain where the water column is well mixed year around; mid-shelf between the 50 m and 100 m isobaths is well mixed in winter but has two distinct layers in summer representing a strong thermocline; outer shelf between the 100 m and 200 m isobaths has both the surface and bottom well mixed layers separated by stratified water in the intermediate depth.

Besides the cross-shelf divisions, the EBS is separated into the northern and southern sub-divisions by 60°N latitude following Stabeno et al. (2012).

3. Results

3.1. Sea ice and EBS shelf bottom temperature

All downscaled simulations in the historical period (1980–2014) capture the observed pattern of mean ice concentration in March (Fig. 2), the month with the most extensive sea-ice cover. In the simulations and satellite observations, sea-ice concentration decreases from the northwest towards the southeast following shelf orientation. Among the ESM forcing ensemble, GFDL forcing produces the closest match with satellite observations, judging by the areas occupied by 90% ice concentration and ice edge location denoted by the 10% ice concentration contour (Fig. 2a-c). All simulated climatological seasonal cycles follow the shape of the satellite-observed seasonal cycle (Fig. 2e), and the EBS averaged March climatology and its interannual standard deviation (from 1980 to 2014) is 0.43±0.16, 0.46±0.12, 0.45±0.16 from CESM, GFDL and MIROC forced simulations, respectively, compared to 0.58±0.18 from satellite observation. Simulated sea ice has less rapid melting than observations in spring, a long-standing issue in sea-ice modeling (e.g. Cheng et al., 2014). Under warming, winter sea-ice fraction on the EBS shelf will decrease significantly (Fig. 3, a-c) while the ice-free season widens (Fig. 3d).

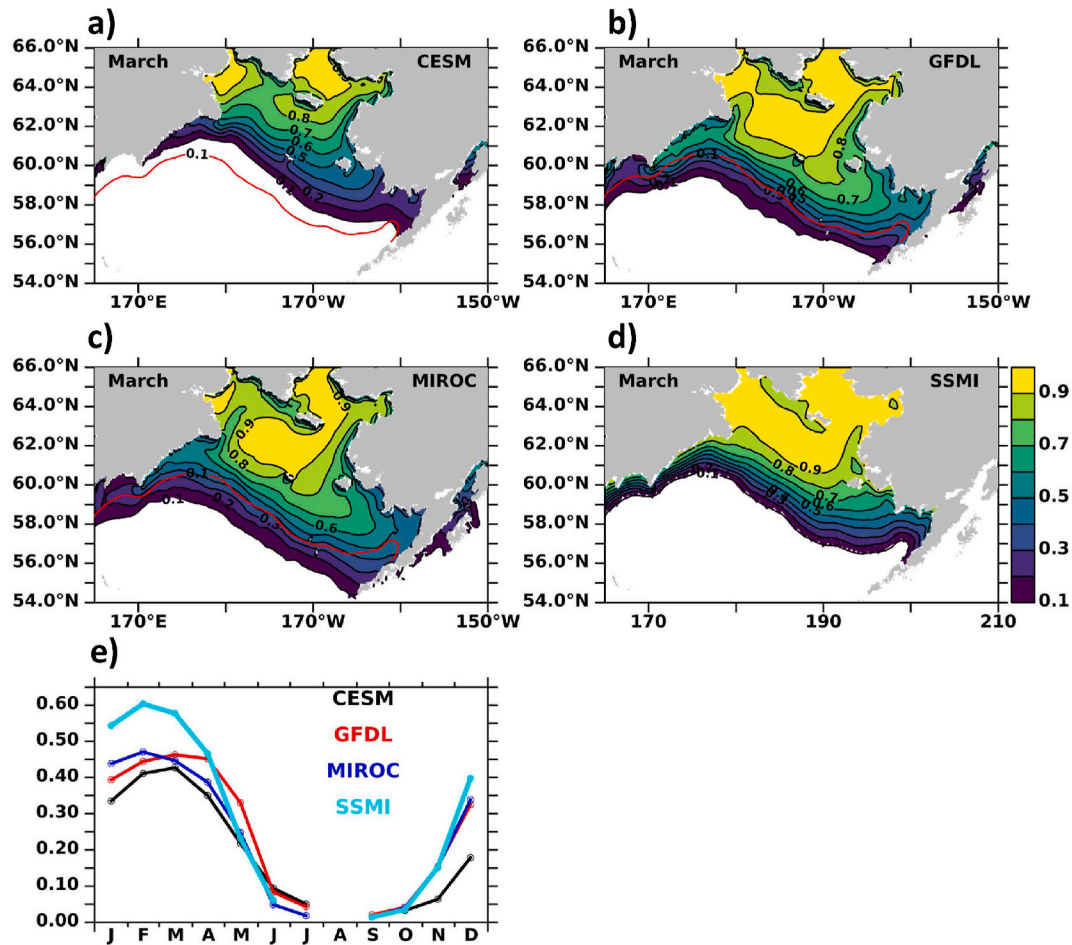Simulated climatology of bottom temperature in July from the his-

Fig. 2. March climatology of sea-ice fraction (dimensionless) from "historical" (1980–2014) simulations (a–c) and satellite SSM/I NASA Team algorithm (d). The red line in a-c denotes the 10% ice fraction contour from the satellite data. Climatological seasonal cycle of ice fraction averaged over areas where ice concentration is not zero (e). Names of global ESMs used to drive Bering10K are indicated on a-c.
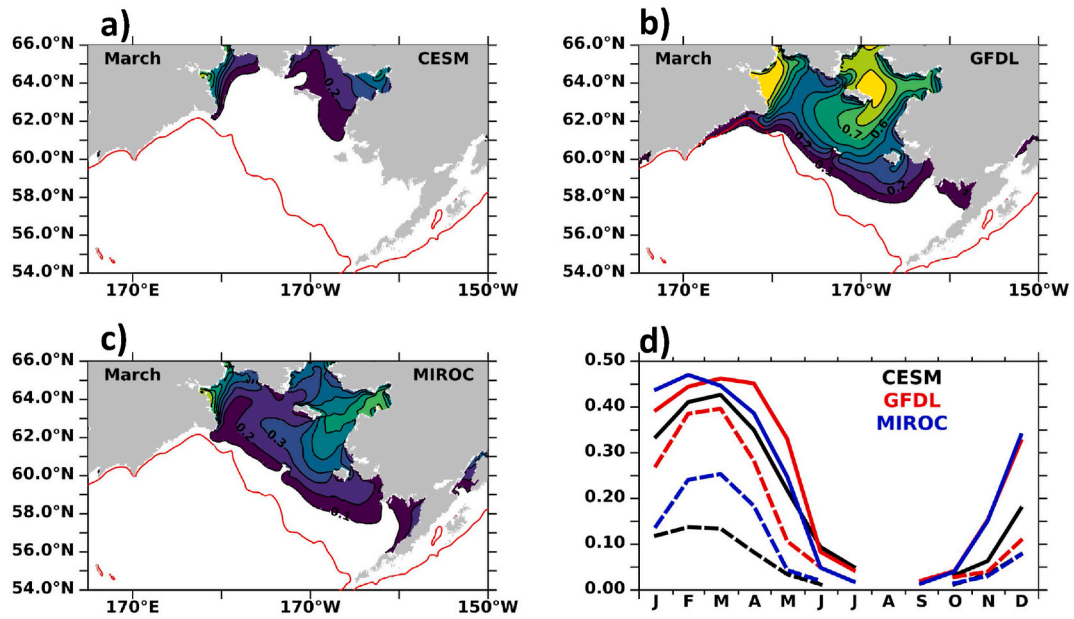
Fig. 3. March climatology of sea-ice fraction (dimensionless) in 2066–2100 under SSP585 forcing (a–c). The red line in a-c denotes the 200-m isobath, and names of the global ESMs used to drive Bering10K are shown on each panel. Climatological seasonal cycle of ice fraction averaged over the horizontal domain shown in a-c (d). Solid (dashed) lines in d) represent monthly climatology based on 1980–2014 (2066–2100).
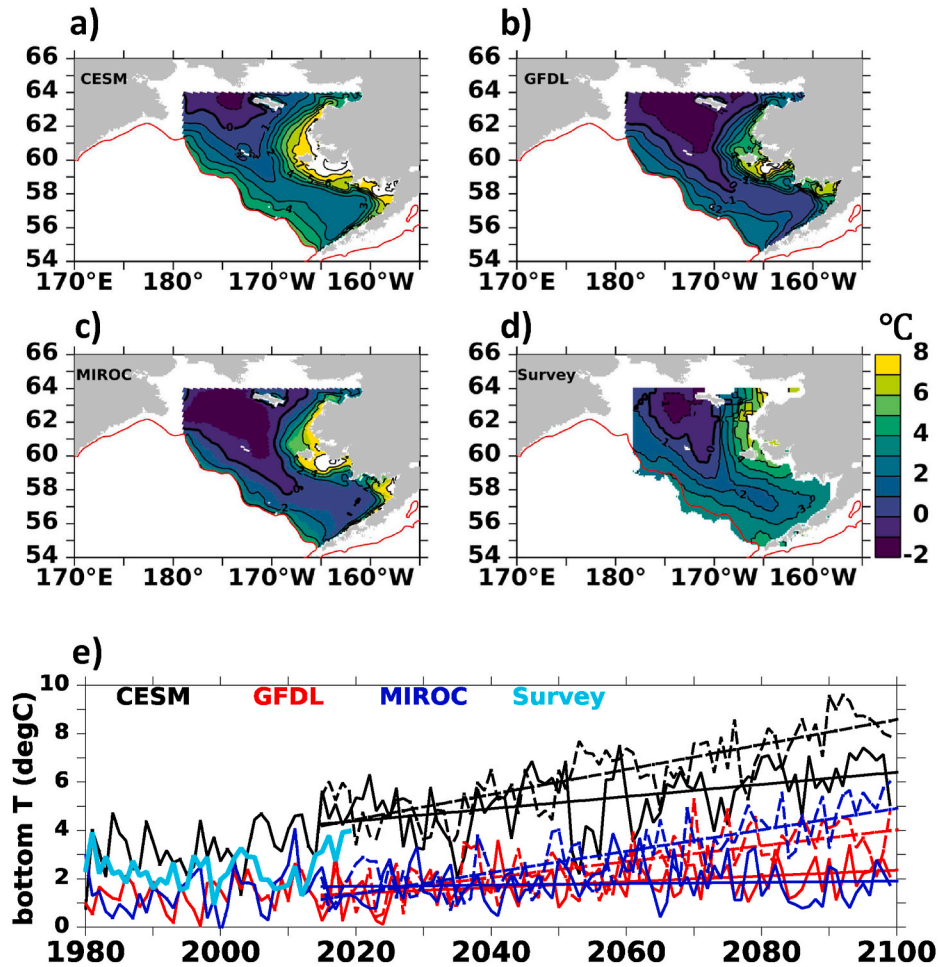

Fig. 4. Climatology of July bottom temperature from Bering10K simulations (a–c) and summer trawl survey (d); July bottom temperature averaged over the Eastern Bering Sea shelf from 1980 to 2100 (e). Climatology in a)-d) is computed from 1980 to 2014. Solid (dashed) lines in e) after 2014 are forced by SSP126 (SSP585) scenarios where the straight lines are the least-square linear regressions of the corresponding time series. Trawl survey in e) spans the years 1980–2019.

torical period captures the corresponding spatial pattern of survey data (Fig. 4) but there are noticeable across-simulation differences – the GFDL and MIROC forced simulations are colder than the observations (comparing Fig. 4 b-c with Fig. 4d) while the CESM forced simulation (Fig. 4a) is warmer: averaged spatially over the EBS (Fig. 4e), 1980–2014 mean bottom temperature and its interannual standard deviation are 3.27±0.95°C, 1.38±0.61°C, and 1.44±0.87°C from CESM, GFDL, and MIROC forcing, respectively, while the corresponding survey value is 2.26±0.62°C. The biases in modeled bottom temperature is consistent with sea-ice extent biases – CESM forcing produces smaller ice extent than observations and a warm bottom temperature bias, while GFDL and MIROC forcings lead to a positive ice extent bias and a cold bottom temperature bias. Nonetheless, all simulations under the SSP585 scenario show significant warming trends from 2015 to 2100 (denoted by the dash straight lines in Fig. 4e) with an amplitude of 0.51°C, 0.32°C, and 0.44°C *per decade* from CESM, GFDL, and MIROC forced simulation, respectively, explaining 67%, 48% and 62% of the corresponding variance (p<0.00001). To summarize, a strong warming trend in EBS bottom temperature is projected by all downscaled simulations under the SSP585 emission scenario. Under SSP126 forcing, CESM and GFDL forced simulations have significant warming trends of 0.25°C and 0.11°C *per decade* respectively (corresponding R^2 is 0.24 for CESM (p < 0.00001) and 0.16 for GFDL (p = 0.0002)) while MIROC forced simulation shows no significant trend.

3.2. Constraint of regional simulation by parent global ESMs

While the high-resolution regionally downscaled simulations are expected to resolve sharper spatial gradients and stronger temporal variability than global ESMs, the degree to which quantities integrated/ averaged over the whole Bering10K domain (both horizontally and vertically) are constrained by parent model forcing versus internal regional model dynamics is not well understood. The relative importance of external forcing (from global ESMs) versus internal dynamics of the regional model is likely process dependent. Presumably, the domain integrals of physical variables from the parent ESMs and dynamically downscaled regional simulations are more likely to be similar to each other than is the case for biological variables, since the governing equations for ocean physics are the same in the global and regional models while there is diversity between the equations used to simulate biochemical processes in the global ESMs and the Bering10K regional model. Results confirm this expectation (Fig. 5). Bering10K whole domain averaged temperatures from the regional simulations almost match exactly with that from the global ESMs (that is, data are situated on the 1:1 diagonal line on Fig. 5a), but there are stronger deviations from the diagonal line in salinity and nitrate concentration (Fig. 5 b-c). Stronger deviations for salinity than for temperature are likely caused by the lack of negative feedbacks between surface freshwater flux and modeled salinity, whereas such feedback exists between surface heat flux and simulated ocean temperature. Larger distance between different colors (representing different ESM) than between the open and filled circles (representing SSP126 and SSP585 forcing within each ESM) also suggests that the across-model spread is stronger than spread across the scenarios, although this result is from a limited size ensemble (N = 3 within each scenario).

Since nitrate concentration is crucial for lower trophic level dynamics, we take a closer look at this variable (Fig. 6). In both the regional and global simulations, the regional domain averaged nitrate concentration decreases with time, but with variable rates. The rate of nitrate decrease in the GFDL forced downscaling is noticeably faster than from the downscalings forced by the other two ESMs (i.e. the vertically oriented data cluster in Fig. 6b), while the GFDL ESM also has the highest nitrate concentration among the three ESMs. It's worth emphasizing that the Bering10K model uses one set of equations and parameters and the only difference across the ESM ensemble is the forcing provided at the lateral boundaries and sea surface. We speculate
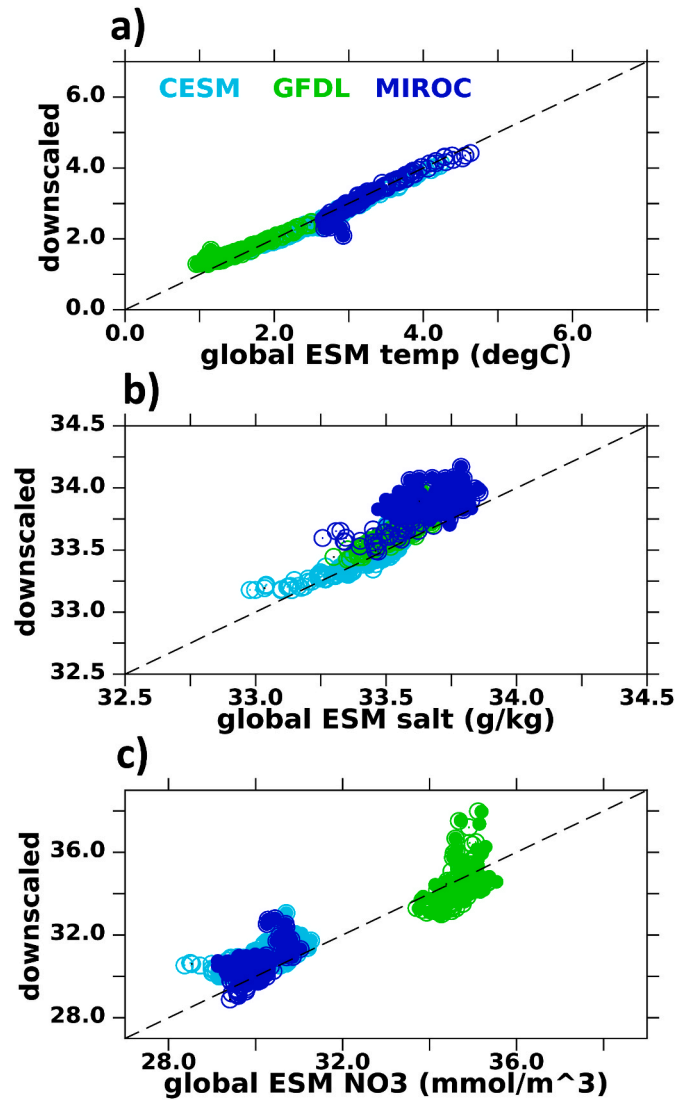

Fig. 5. Scatter plot of full Bering10K domain averaged ocean temperature (°C), salinity (g/kg), and nitrate concentration (mmol/m³) in March directly from global ESMs (using the horizontal axis) vs. from the downscaled Bering10K regional simulations (using the vertical axis). Different colors correspond to different ESMs and their downscaled results (color legend is shown in panel a). Filled (open) circles are from historical + SSP585 (historical + SSP126).

that the faster nitrate decline in the GFDL forced simulation reflects the regional simulation adjusting towards its own preferred state subject to regional model formulation, but more work is needed to confirm this hypothesis.

3.3. Bering10K full domain vs. EBS shelf stratification

To evaluate Bering Sea hydrographic changes, we use stratification quantified by brunt-vaisällä frequency $N^2 = -\frac{g}{\rho}\frac{d\rho}{dz}$ (units: $1/s^2$) as it impacts a suite of biological processes ranging from nutrient transport to sinking of particles. Averaged over the Bering10K horizontal domain, stratification increases with time (Fig. 7): specifically, anomalies relative to the 1980–2014 mean state averaged over 2066–2100 and from surface to 200-m depth are 2.0, 1.1, and 1.7 (units: 1.e-5 $1/s^2$) under the CESM, GFDL, and MIROC SSP585 forcing respectively, which is 49.1%, 23.4%, and 33.0% of their 1980–2014 mean N^2. Consistent with its weaker bottom temperature warming trend relative to the other two models (Fig. 4), the GFDL forcing also produces the weakest
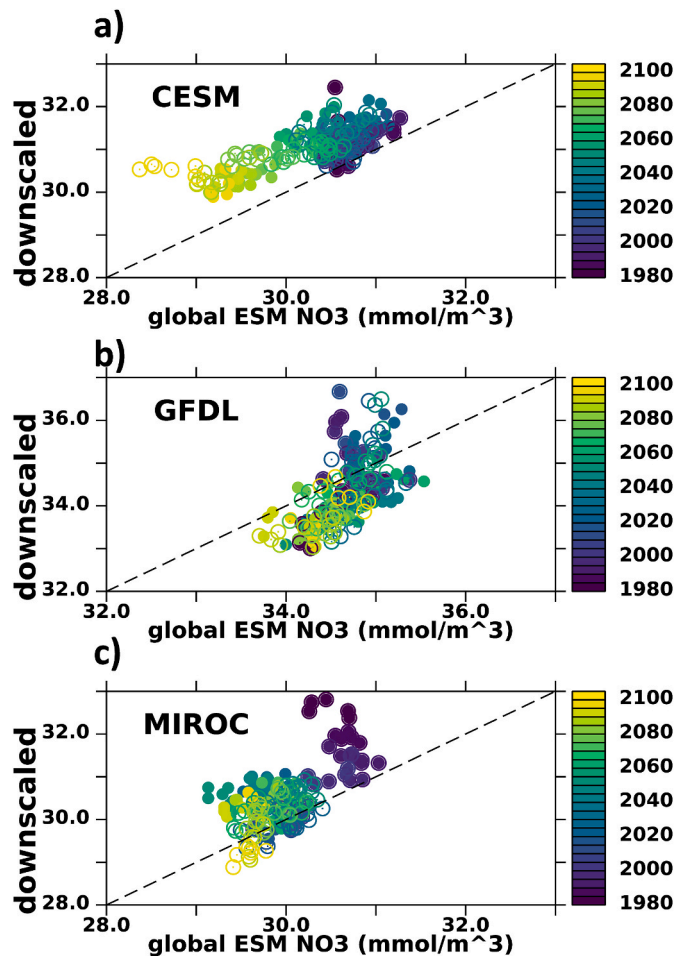
a)

b)

c)

Fig. 6. Same as Fig. 5 but only for nitrate concentration (mmol N/m^3), and results from different ESMs are displayed in separate panels. Symbols are colored coded by year from 1980 to 2100. Ranges of the vertical and horizontal axis are the same in a)-c).

stratification increase among the three simulations, and GFDL forced positive temperature anomalies penetrate to shallower depth than those forced by the other two ESMs. Within each ESM, the difference in stratification increase between SSP126 and SSP585 scenarios is evident after mid-century (~2050) but minimal in the earlier decades.

The above full domain average patterns of water column stratification change when we repeat our analysis using only the EBS; in that case, summer stratification below the surface mixed layer weakens under climate forcing, especially in the GFDL and MIROC forced simulations (Fig. 8). This is related to the loss of sea ice and ice melt induced freshwater stratification on the Shelf. As shown in Section 3.1, the Bering Sea shelf is seasonally covered by sea ice historically (Fig. 2), but sea-ice concentration in winter will decrease significantly with warming (Fig. 3). In January, salinity anomalies (future climatology minus historical climatology) on the shelf are negative from the sea surface to the bottom (Fig. 9a-b), consistent with both increased surface freshwater flux into the ocean and melting of sea ice under climate forcing (Lee et al., 2013) and facilitated by strong mixing during winter. In addition, fresher bottom water is projected south of the Alaskan Peninsula (Fig. 9b, 9d), and this water flows through Unimak Pass and enters the southeastern Bering Sea shelf thus serving as a source of fresher bottom water (Stabeno et al., 2002). In July, however, the projected sea surface salinity (SSS) anomaly is positive in the northern shelf (Fig. 9c) but remains negative at depth (Fig. 9d). The positive SSS anomaly in summer in the future is associated with lack of ice melt induced freshening. Similar processes have been observed in the Bering Sea under recent ice

loss events (Stabeno and Bell, 2019). Lack of sea ice and ice melt in the future contributes to weakened freshening in the upper layers relative to the lower layers, when averaged over the shelf during the summer months (Fig. 9f). This unique vertical gradient of salinity changes - stronger freshening at the lower than upper layers on the shelf - is largely absent from the Bering10K full domain average (Fig. 9e) and contributes to the subsurface stratification decrease for the EBS Shelf shown in Fig. 8. This result is consistent with Lee et al. (2013) where stratification of the upper layer (0–60 m) in June weakens and the mixed layer deepens in the shelf region under a 1% per year CO_2 increase experiment.

3.4. Lower trophic level responses to climate forcing

3.4.1. Historical mean states

As a baseline against which future changes are assessed, monthly climatology of water column biophysical variables averaged on the Bering Sea shelf in the historical period (1980–2014) are provided in the supplemental material. These state variables exhibit strong seasonal cycles with distinct vertical patterns. For example, potential temperature is generally well mixed in winter across the entire shelf but stratifies in summer while salinity shows a vertical gradient yearly around but stronger gradient in summer than in winter (Fig. S1). Nitrate distribution indicates upper layer drawdown and depletion during the growth season while ammonium concentration peaks at depth in the fall following spring and summer growth (Fig. S1). A distinct feature in the distribution of both phytoplankton size classes is the presence of a subsurface maxima, which appears near the base of the mixed layer subsequent to the initial surface bloom (Fig. S2). This subsurface biomass maximum is driven primarily by regenerated production and extends further into the growing season than surface biomass. Increased ammonium uptake in late summer and fall is also suggested by observations made in Canadian Arctic waters (Martin et al., 2012). Oxygen seasonal cycle and vertical distribution is influenced by phytoplankton growth and respiration and also regulated by ocean temperature and air-sea exchange – it peaks at the same time/depth as the phytoplankton biomass maximum but remains relatively high in winter due to both strong exchange with the atmosphere in ice-free waters and increased solubility under cold temperatures (Fig. S2). The near-surface and near-bottom minimum in the summer and fall oxygen concentration is associated with decreased solubility and increased respiration as biomass sinks to the bottom. The seasonal cycle and vertical distribution of different zooplankton classes (Fig. S3) are similar to those of the phytoplankton size classes, with zooplankton vertical distribution primarily being a function of the location of their prey. An exception to this is seen within the large-bodied copepod functional groups (Fig. S3, "NCaO" and "NCaS"). These groups migrate down to depth up to ~400 m in late summer of the year to reflect the diapause phenomenon, and their biomass values subsequently decrease due to lack of spatial overlap with their prey groups. The on-shelf ("NCaS") group is able to maintain a small population at depth, with a small secondary peak in July and August, while the oceanic (NCaO) group is programmed to die once they reach the bottom.

3.4.2. Spatiotemporal characteristics of projected changes

To illustrate future changes, we present monthly climatology anomalies (climatology from 2066 to 2100 minus that from 1980 to 2014) of phytoplankton biomass, zooplankton biomass, nitrate, and oxygen under SSP585 forcing (Fig. 10). Anomalies of plankton biomass and oxygen are depicted at coordinate vertical level 18, which has a mean depth of 12 m averaged over the shelf region (keep in mind that depth of layer 18 in terrain-following vertical coordinate is a function of ocean bottom depth and is shallower where the ocean bathymetry is shallower, and vice versa) and approximates the location of the subsurface maxima across much of the southeastern shelf in the historical climate (Fig. S1-S2) as well as the layer with the largest changes in the
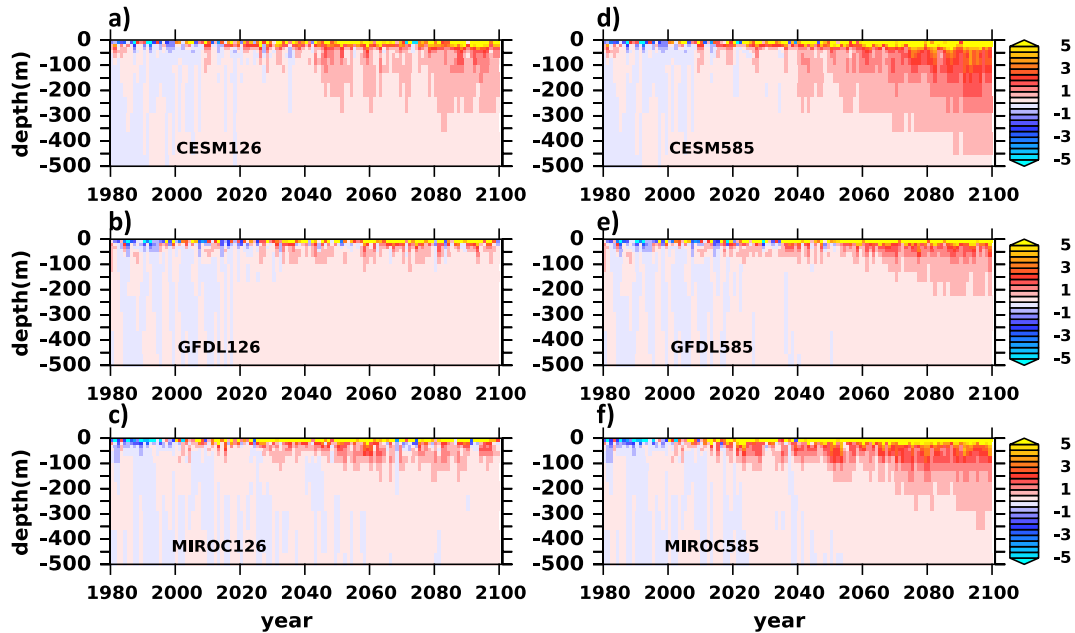
Fig. 7. Changes in July Brunt-Väisälä frequency (N^2, unit: 1.0e-5 s^{-2}) relative to 1980–2014 mean. Names of the global ESM and SSP scenarios are indicated on each panel. Results are averaged over the full Bering10K domain (Fig. 1a), and y-axis corresponds to the mean depth of Bering10K vertical layers (from surface to layer 17) averaged over this domain.
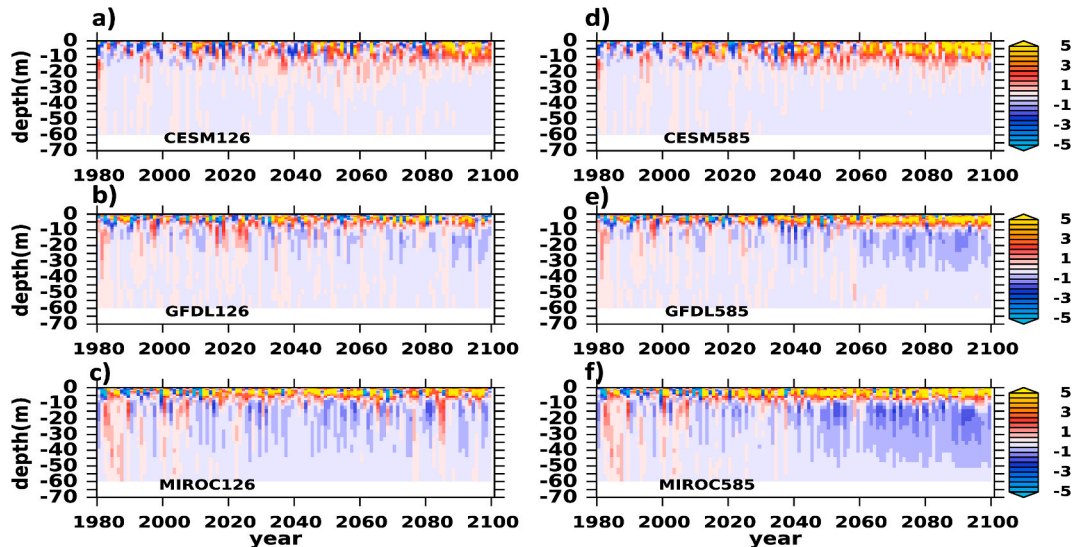

Fig. 8. Same as in Fig. 7 but averaged over the Bering Sea shelf only (Fig. 1d), and results are shown for the entire water column from surface to bottom.

future (Fig. 10 a-d, bottom row). Anomalies of nitrate are shown for the bottom layer.

In April–May, phytoplankton biomass shows widespread positive anomalies across the portion of the shelf that was covered by seasonal ice in the historical period, while historically ice-free regions (southernmost portions of the middle and outer shelf) experience negative anomalies. In July–August, phytoplankton biomass anomalies are generally negative shelf-wide, with small changes across the outer-middle domain but larger decreases in the inner domain (Fig. 10 a). Zooplankton biomass anomalies show a similar pattern at this layer, with positive anomalies in spring and negative anomalies in summer (Fig. 10b, top two rows). Averaged over the entire shelf, phytoplankton and zooplankton anomalies are positive at all layers before May and negative thereafter (Fig. 10 a-b, bottom row). These patterns of biomass anomalies suggest a phenological shift toward earlier blooms.

Similar to biomass changes, nitrate and oxygen concentrations have negative anomalies throughout the annual cycle and at most layers (Fig. 10 c-d), with exception at the northern shelf for oxygen concentration. The vertical distribution of oxygen anomalies (Fig. 10c, bottom row) is pattern-correlated with that of phytoplankton biomass (Fig. 10a, bottom row) with a correlation coefficient of 0.77 (p < 0.0001). Averaged nitrate concentrations show a future decrease throughout the entire water column before the spring drawdown (Fig. 10d, bottom row) with decreases as large as 10 mmol N/m^3 on the southeastern shelf (Fig. 10d, top row). Nitrate input at the Bering10K lateral boundaries has no significant trend over the simulation period (not shown), suggesting that the nitrate concentration changes on the EBS shelf (Fig. 10d) are regulated primarily by internal dynamics of the regional model, but more work is needed to identify the precise mechanisms.

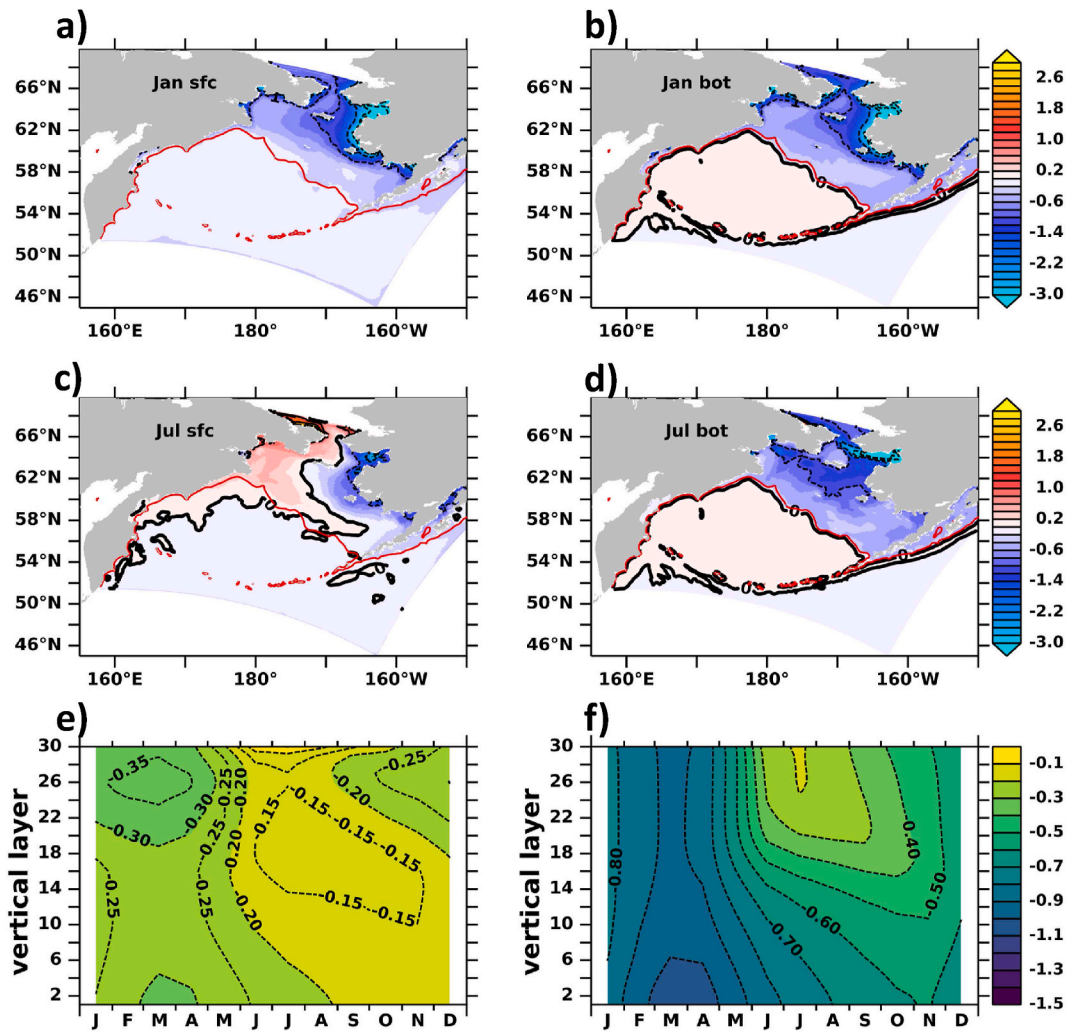The phenology shift in plankton biomass is also seen when

Fig. 9. Ensemble mean (averaged over three ESMs) changes in monthly climatology from 2066 to 2100 relative to that of 1980–2014 under SSP585 forcing (later minus earlier climatology). Shown are sea surface salinity anomalies (g/kg) in January (a) and July (c), bottom layer salinity anomalies in January (b) and July (d), vertical distribution of salinity anomalies averaged over the full Bering10K domain (e) and EBS shelf only (f). Red contours in (a)-(d) represent the 200-m isobath. Y-axis in (e–f) corresponds to the vertical coordinate layer of the model (K = 30 is at the sea surface).

comparing monthly climatology from different time periods in individual shelf biophysical domains though there are across-region differences (Figs. 11 and 12). In all time periods seasonal phytoplankton biomass decreases from inshore to offshore with subtle differences in the north-south direction (Fig. 11a). For instance, the southern shelf could have a secondary peak around October (Fig. 11a, panels labeled as "s-inn" and "s-mid") but this signature is weaker in the northern shelf. This is consistent with previous observations (Sigler et al., 2014) and modeling studies (e.g. Cheng et al., 2016; Kearney et al., 2020) where rapid *in situ* nutrient recycling is found to contribute to a fall bloom in the southern shelf. On the other hand, the spring phenology shift of phytoplankton biomass appears stable in the south particularly in the middle and outer domains where no significant biomass growth develops prior to April in all time periods (Fig. 11 b, lower row, left two panels). Predictions of enhanced late winter to early spring biomass in the north are likely due to enhanced light availability associated with sea-ice reduction and temperature increase in the future. Sea-ice reduction is not nearly as strong in the south, resulting in a more subtle shift in biomass growth timing. The relative decrease in the future fall phytoplankton biomass climatology is comparable across all shelf biophysical domains and is about 50% of their corresponding historical climatology (value of the teal lines in August–October in Fig. 11b), suggesting potential roles of processes that influence nutrient supply to the entire EBS shelf rather

than advective processes within the shelf that redistribute nutrients locally.

The phenology shift is seen in large zooplankton biomass as well (Fig. 12). Specifically, in the south-inner domain, spring biomass increase occurs approximately one month earlier in 2066–2100 than in 1980–2014, while the fall decrease occurs 2 months earlier. The associated changes in standing biomass in a given month/domain are significant. For instance, on the south-inner shelf, mean biomass in April (October) of the 2066–2100 climatology under SSP585 forcing is three times (half) of their historical values (Fig. 12b, lower-right panel). Incidentally, the averaged seasonal cycle under SSP126 from both 2031–2065 and 2066–2100 is close to the averaged seasonal cycle of 2031–2065 under SSP585 forcing (Fig. 12a, closeness of the dashed lines to the solid gray line), whereas the seasonal cycle from 2066 to 2100 under SSP585 (Fig. 12a, teal solid line) has shifted significantly from the other three cases. By this metric, less intense forcing (SSP126) has delayed the phenology shift from strong forcing (SSP585) by ~35 years.

3.4.3. Model and scenario uncertainties

Uncertainty in future projections is generally attributed to three sources (e.g. Hawkins and Sutton, 2009): 1) natural/internal variability of the climate system; 2) model structural uncertainty; 3) scenario uncertainty. In the dynamical downscaling framework where one regional
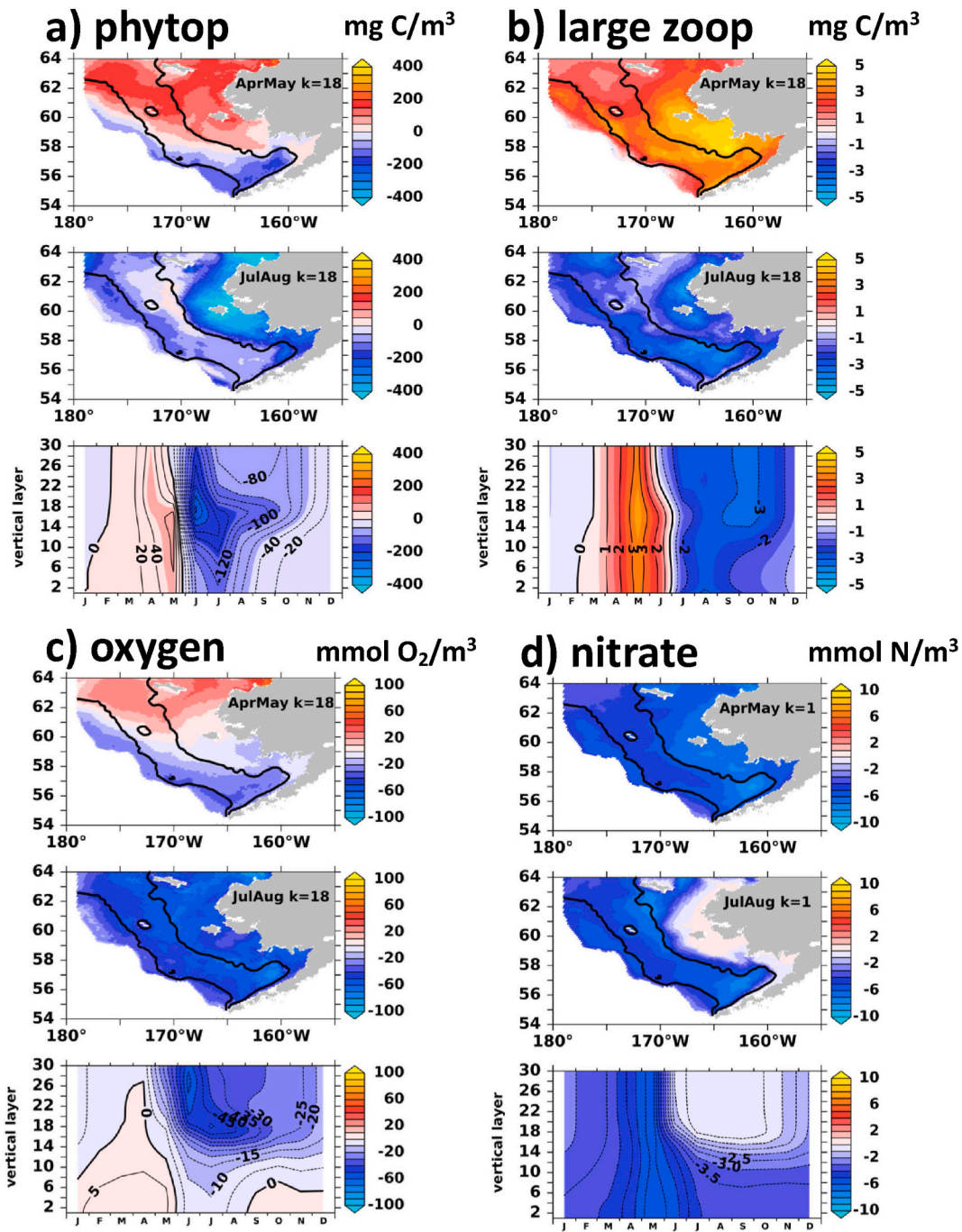
Fig. 10. Changes in monthly climatology of the multi-model mean from 2066 to 2100 relative to that from 1980 to 2014 (later minus earlier climatology) under SSP585 forcing. Shown are a) subsurface phytoplankton biomass (mg C/m³), b) subsurface large zooplankton biomass (mg C/m³), c) subsurface oxygen (mmol O₂/m³), and d) bottom nitrate concentration (mmol N/m³). In a)-d), the first (second) row is averaged over April–May (July–August) representing the spring (fall) growth season; the third row shows the corresponding monthly climatology anomalies averaged horizontally over the EBS displayed as a function of vertical co-ordinate layer (k = 30 is at the sea surface) and month.

biophysical model is used, model uncertainty is associated with the parent global ESMs. The relative amplitudes of model versus scenario uncertainties have been quantified in numerous studies (e.g., Hawkins and Sutton, 2009; Frölicher et al., 2016) and the results are found to be dependent on the processes in question. For instance, in terms of global mean temperature increase, scenario uncertainty generally surpasses model uncertainty in the 2nd half of the 21st century (Hawkins and Sutton 2009); in contrast, projections of net primary productivity (NPP) are dominated by model uncertainty even at the end of 21st century (Frölicher et al., 2016). While our ensemble size is limited, we can

quantify model vs. scenario uncertainties to inform future model and scenario selections for dynamical downscaling, as there are tradeoffs between using more global ESMs vs. more scenarios.

We first analyze the large zooplankton biomass as it represents a key stepping stone between lower trophic level components and fisheries. Model uncertainty is quantified as the standard deviation around the multi-model mean and presented in Fig. 13 for the shelf biophysical domains, separately for the spring growth, fall decrease, and over-wintering seasons. Under SSP585 forcing, model uncertainty generally increases towards the shore, and it is larger in the fall season than in
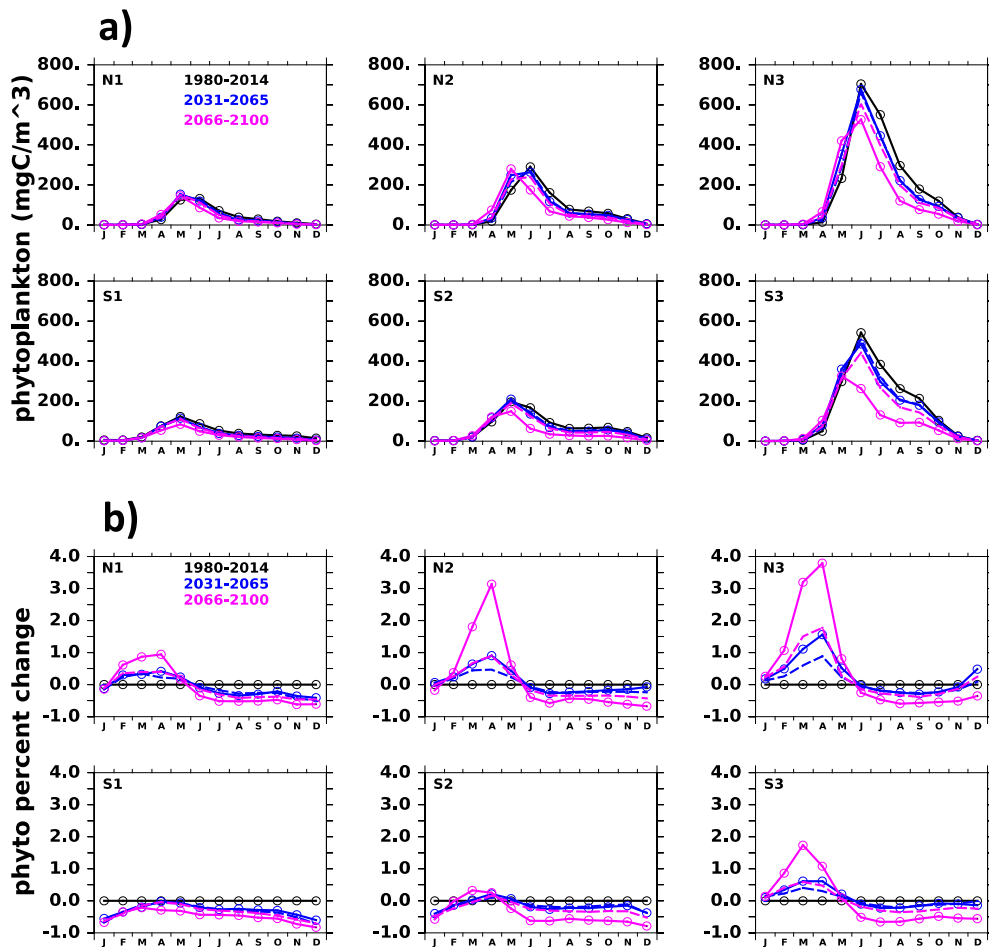
Fig. 11. Ensemble mean of monthly climatology of phytoplankton biomass (units: mg C/m^3) from "historical" (green lines), mid-century (gray lines) and late 21st century (teal lines) simulations (a). Same as in (a) but showing fractional changes of future climatology relative to historical climatology defined as (climo_future - climo_historical)/climo_historical (b). Results are averaged vertically and horizontally over each biophysical domain of the EBS shelf whose names are indicated by y-axis labels. Solid (dashed) lines are forced by the SSP585 (SSP126) scenario.

spring. This suggests that there is more uniformity in global ESM's treatment of spring bloom dynamics (e.g. processes that determine light availability) than in their representation of processes that control fall productivity dynamics such as nutrient recycling (i.e. mixing and regeneration). Despite these uncertainties, across all shelf domains, spring (fall) large zooplankton biomass increases (decreases) with time, reflecting the phenology shift described above. Model uncertainty characteristics under SSP126 forcing (Fig. S4) is qualitatively similar to that under SSP585 forcing and SSP126 produces overall weaker trends than SSP585.

Ensemble averages of SSP585 and SSP126 projections, respectively, of the biophysical variables on the EBS shelf do not diverge significantly from one another until 2070 (Fig. 14), even then there are still overlaps between the two scenarios given the large across-model spread (Fig. 14). This is consistent with the weak scenario spread seen in Figs. 5, 6, 11 and 12. Our results from a limited set of ESM ensembles corroborate the conclusions of Frölicher et al. (2016) where it is found that for NPP, global ESM structural uncertainty is larger than scenario uncertainty at the end of the 21st century across the CMIP5 ensemble. These results therefore advocate for the use of highly contrasting SSP scenarios in dynamical downscaling aimed at understanding lower trophic level responses to climate forcing on the EBS shelf. The percent decrease of these processes averaged in 2066–2100 relative to historical mean states in 1980–2014 is summarized in Table 2.

4. Discussion

In the previous CMIP5 downscaling of the Bering Sea under Representative Concentration Pathway 8.5 forcing scenario, which is

comparable to SSP585 in CMIP6, Hermann et al. (2019) found that the averaged shelf bottom temperature may warm by as much as 5°C by 2100. This result is largely unchanged in the CMIP6 driven ensemble suite, especially considering the large uncertainties associated with the across-model spread (Fig. 15 a). In terms of biomass changes, results from Hermann et al. (2019) using the previous Bering10K with ten layers and CMIP5 forcing (Fig. 15, b-c, red lines and shading) are similar to results from this study using the updated Bering10K biogeochemistry and CMIP6 forcing (Fig. 15, b-c, black lines and shading). A noticeable change between Hermann et al. (2019) and this study is the increased across-model spread in the CMIP6 forced projections. This is consistent with larger spread of ECS among the CMIP6 models we used than among the CMIP5 models (highest minus lowest ECS among CMIP6 is 2.49, compared to 2.21 among CMIP5) (Table 2). The same Bering10K biogeochemistry as used in this study but under CMIP5 RCP8.5 forcing (Pilcher et al., 2021, this issue) produced larger mean biomasses, but their declining trend under warming is similar to both Hermann et al. (2019) and this study (Fig. 15, b-c, blues lines and shading). Similarities as well as differences in the dynamically downscaled long-term projections across CMIP generations are expected, and they reflect structural differences in global ESM and the regional model formulation. Our results highlight the large uncertainty associated with using a limited number of parent models for dynamical downscaling. Hybrid methods combining dynamical and statistical downscaling are possible ways to efficiently increase regional downscaling ensemble size (Hermann et al., 2019; Hermann et al., this issue). The strength and weakness of each statistical method (e.g. combined EOF analysis, linear inverse modeling) and the underlying assumptions are areas that need further research.

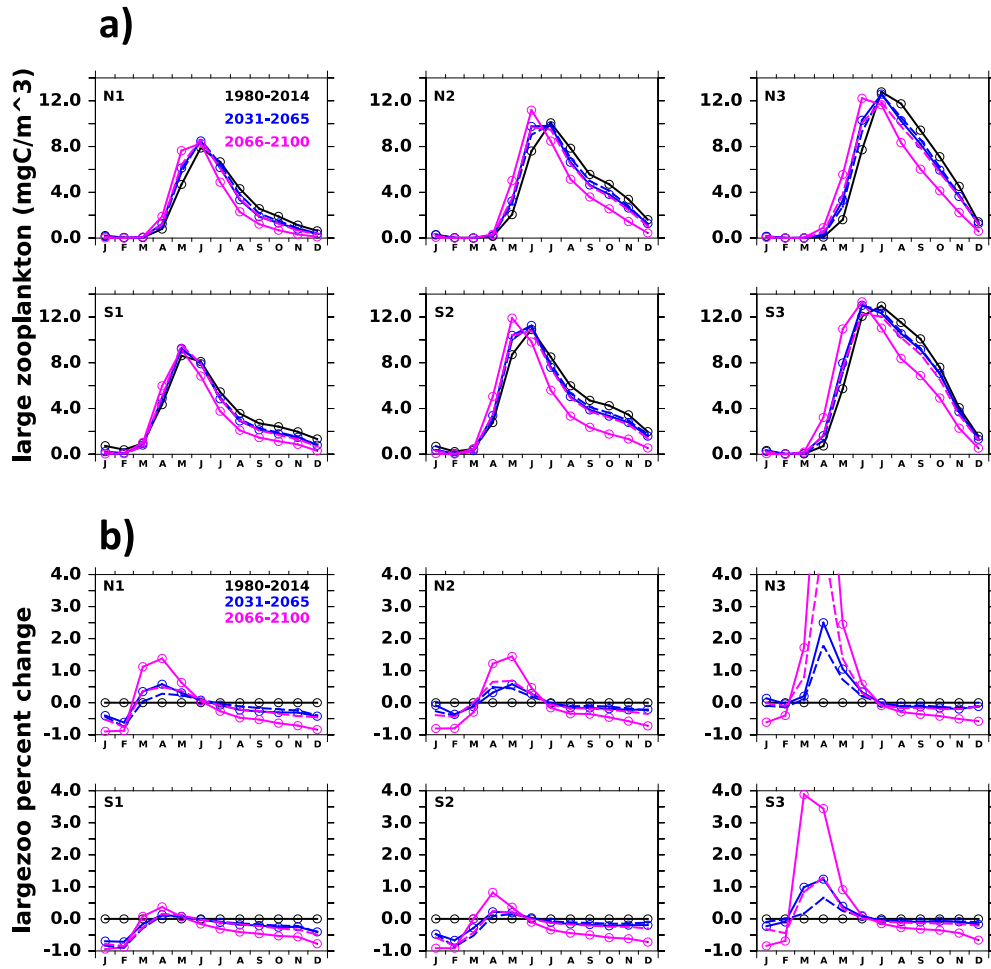On the global scale, climate projections suggest that under warming,

Fig. 12. Same as Fig. 11 but for large zooplankton biomass (units: mg C/m³). The maximum value for the northern inner shelf on b) is out of y-axis range and approaches 10. This high value is because April climatology of zooplankton biomass in this region is small for the historical period.
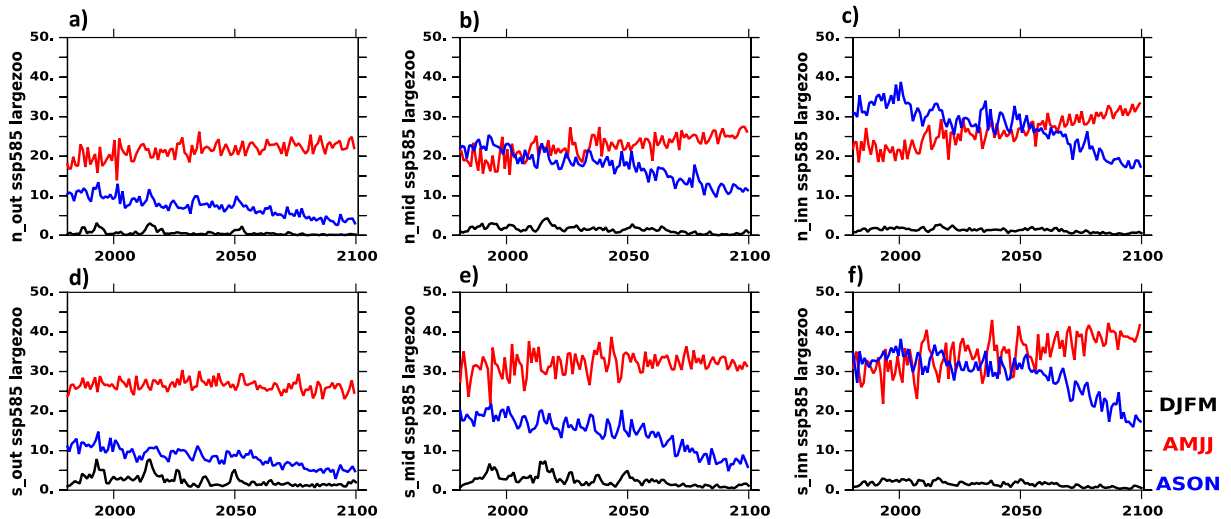

Fig. 13. Annual mean time series from 1980 to 2100 of the vertically averaged large zooplankton biomass (units: mg C/m³) in each of the EBS shelf biophysical domains. Solid lines are ensemble means and shading represents ± one standard deviation of ensemble spread around the ensemble mean. Future projections are forced by the SSP585 scenario. Black, red, and blue color corresponds to December-to-March (DJFM), April-to-July (AMJJ), and August-to-November (ASON) averages, respectively.

primary productivity in the tropics and mid-latitudes will decrease due to weakened mixing bringing less nutrients to the surface euphotic zone, while in the high latitudes, primary productivity will increase because

weakened mixing and reduced sea ice alleviates light limitation (e.g., Bopp et al., 2013; Kwiatkowski et al., 2020). For the EBS phytoplankton projections, competing effects are at play, e.g. rising temperature
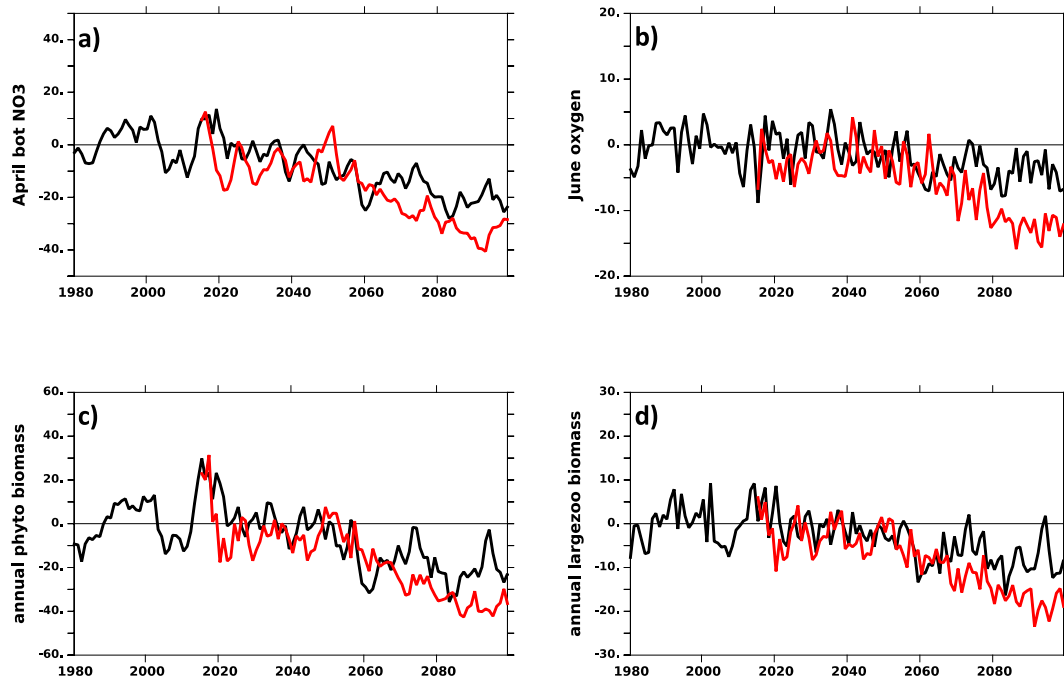
Fig. 14. Percent changes in future projections relative to historical (1980–2014) mean state, results are horizontally averaged over the EBS shelf. (a) April bottom layer nitrate concentration (mmol N/m³); (b) July layer 18 oxygen concentration (mmol O2/m³); (c) annual mean vertically averaged phytoplankton biomass (mg C/m³); (d) annual mean vertically averaged large zooplankton biomass (mg C/m³). Black (red) line after 2014 is forced by the SSP126 (SSP585) scenario. Solid lines are ensemble means and shading represents ± one standard deviation of ensemble spread around the ensemble mean.

Table 2
Percentage changes in the 2066–2100 mean values relative to the 1980–2014 mean values of various biological variables spatially averaged over the Eastern Bering Sea shelf under SSP126 and SSP585 forcing. Results listed are the multi-model mean ± across-model standard deviations around the multi-model mean.

	SSP126	SSP585
June layer 18 oxygen	-3.71±4.79	-10.34 ± 4.54
April bottom NO3	-18.09 ± 7.72	− 29.40±6.03
Annual phytoplankton biomass	− 18.77±9.67	− 32.27±8.16
Annual large zooplankton biomass	− 7.15±4.81	− 15.11±4.08

increases biological growth rate and promotes primary production on the one hand (Brown et al., 2011), and warming/increased stratification decreases nutrient supply and primary productivity on the other (Strom and Fredrickson, 2008). Loss of sea ice affects this balance as well, by

increasing light penetration and reducing the seasonal stratification associated with ice melt. The relative importance of sea-ice loss and temperature increase on ocean primary production changes is discussed in Gibson et al. (2020), and the results are found to vary strongly by region. Our dynamical downscaling results under CMIP5 and CMIP6 forcing both suggest that the annual mean phytoplankton biomass on the Bering Sea shelf will decrease, accompanied by a spring biomass increase and fall biomass decrease associated with a phenology shift. The phenology shift is detected when comparing future climatology based on years 2031–2065 or 2066–2100 with historical climatology from 1980 to 2014, and this signal emerges despite interannual variation observed in recent years where anomalously warm years with early ice retreat are associated with delayed spring bloom. Regional downscaling results are subject to the particular formulation of Bering10K and its parameters. In the future, systematic contrasting between the global ESM and Bering10K projections and identification of underlying causes
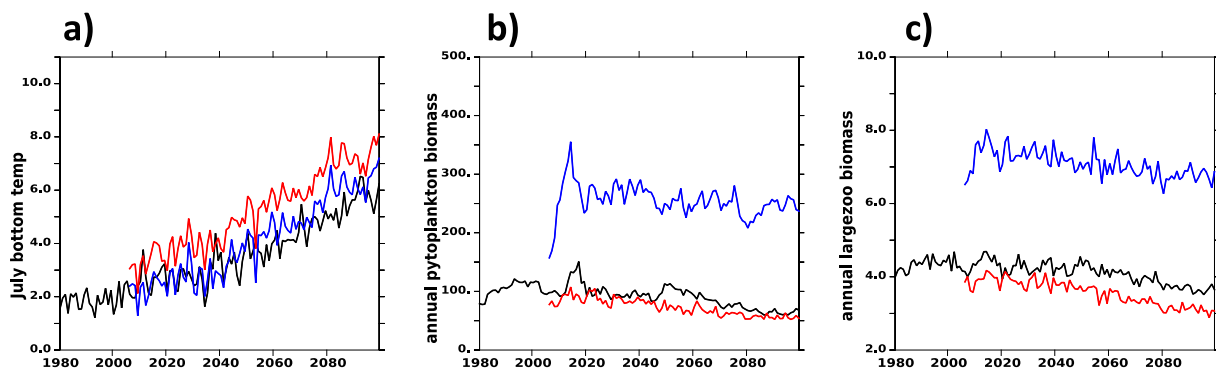

Fig. 15. Comparison across CMIP5 and CMIP6 Bering10K downscaled simulations. Shown are EBS shelf July bottom temperature (a, unit: °C), vertically averaged annual mean phytoplankton (b) and large zooplankton biomass (c, unit: mg C/m³). Lines are ensemble means averaged across ESM forcings and shading represents ± one standard deviation of ensemble spread around the ensemble mean. Black, red, and blue color corresponds to result from 30-layer Bering10K forced by CMIP6 ESMs (this study), 10-layer Bering10K forced by CMIP5 ESMs (Hermann et al., 2019), and 30-layer Bering10K forced by CMIP5 ESMs (Pilcher et al., 2021, this issue), respectively. Forcing from CMIP5 (CMIP6) ESMs is RCP8.5 (SSP585).

for significant differences or lack thereof will be informative. Global and regional projections provide complementary information - the former is a coordinated multi-national, multi-institution effort which allows for better quantification of natural, model structural, and scenario uncertainties, while the latter tends to be carried out by a single institution and provides regional user-relevant information. The complexity of marine ecosystem dynamics likely demands continued usage of both modeling approaches in the future.

Impacts of warming on phytoplankton seasonality have been previously examined in CMIP5 models (Henson et al., 2013). In the oceanic biogeographic "province" of the high latitude North Pacific (which includes the Gulf of Alaska and Bering Sea), Henson et al. (2013) found a negative trend in primary production with large inter-model uncertainties and an earlier timing of seasonal primary production peak. This is consistent with our downscaling results although we focus on a much smaller geographic region. Seasonality shifts in these latitudes are generally attributed to reduction in mixing, which leads to earlier removal of light limitation and an earlier start to the growth season (e.g. Doney, 2006). Henson et al. (2013) also detected a negative trend in surface nitrate concentration in the same ocean province, again consistent with our results. In the regional dynamical downscaling framework, nitrate concentration on the Bering Sea shelf is influenced by the internal dynamics of the regional model as well as external forcing of macronutrient concentrations imposed at the lateral boundaries. Preliminary results suggest that the trend in the lateral boundary forcing from the global ESMs is weak through 2100, but a more comprehensive nutrient budget analysis of the Bering Sea shelf is needed to shed light on the precise mechanisms that control EBS shelf nutrient sources and sinks, and to separate spin up-induced drift from climate change impacts.

Subsurface phytoplankton biomass maxima are a common feature in model simulations and *in situ* observations, but they may not be fully captured by satellite remote sensing which suggests an increase in NPP for Arctic ecosystems under warming and reduced ice (Arrigio et al., 2008). Model simulations can be used to investigate the subsurface maxima formation mechanisms and relationships between phytoplankton biomass vertical structure and its surface imprints, and how these relationships may change under climate forcing. While we have qualitative knowledge on how ocean temperature, stratification/light limitation and nutricline may adjust to climate forcing and how these processes affect phytoplankton vertical distribution (Cullen, 2015), quantification of these complex interactions is only possible with more complete observations and data validated model simulations.

Here we have presented results from a limited ensemble dynamical downscaling and focused specifically on the EBS shelf through the lens of a few ecosystem critical biophysical processes. With their caveats, these modeling results reiterate the strong spatiotemporal heterogeneity in the shelf ecosystem response to climate forcing. Undoubtedly marine ecosystems will experience multiple stressors under warming (Bopp et al., 2013), and such signals are likely more acute on the regional scales. The implications of these changes on the upper trophic level and fisheries processes are currently addressed through the integrated ACLIM project (Hollowed et al., 2020; Holsman et al., 2020).

5. Conclusions

In this study, we analyze the latest Bering Sea dynamical downscaling simulations forced by selected CMIP6 ESMs. These simulations comprise the lower trophic modeling component of the ACLIM project, where regionally downscaled biophysical indices are used in a suite of ecosystem modeling experiments with an ultimate goal of evaluating fishery management strategies. Therefore, we focus on analyzing shelf biophysical variables that potentially affect the upper trophic level marine ecosystem and fisheries. The main conclusions from this study are:

1) Volume integrated ocean hydrography and nitrate concentration of the regional simulations are constrained by parent ESM forcing to varying degrees. More specifically, domain averaged temperature of the regional simulations mirror those in the global ESMs whereas the corresponding salinity and nitrate concentration show stronger deviations from the parent ESMs (Figs. 5 and 6).

2) Ocean stratification response to climate forcing averaged over the Bering10K full domain (including the shelf and deep basin) differs from that averaged on the shelf (Figs. 7 and 8). This is because summer stratification on the EBS shelf is influenced by ice melt induced freshening. Loss of sea ice in the future diminishes its surface freshening effect during the melt season, reducing negative sea surface salinity anomalies and weakening stratification (Fig. 9). In this sense, loss of sea ice (a winter phenomenon) has non-contemporaneous consequences (affecting summer stratification).

3) Modeled primary and secondary plankton biomass has subsurface maxima during the growing season whose amplitude decreases with warming. Accompanying warming and primary productivity change, oxygen concentration decreases over much of the Bering Sea shelf water column, and the vertical and seasonal adjustment of oxygen concentration is pattern correlated with phytoplankton biomass changes (Fig. 10).

4) Across the EBS shelf, phenology of phytoplankton and zooplankton biomass shifts earlier (Figs. 11 and 12), and shifts are stronger on the inner and middle domains than on the outer domain, and in the northern latitudes (north of 60°N) than in the south. The corresponding fall plankton biomass decrease has a larger across-model spread than the spread in the projected spring biomass increase (Fig. 13).

5) Projections of regional biogeochemistry adjustment at the end of the 21st century are not well separated between SSP126 and SSP585 forcing given the large across-model spread within each scenario (Fig. 14). This result, albeit from a limited ensemble size (three ESMs under each scenario), is consistent with an earlier study using more global ESMs where inter-model spread is found to be larger than scenario spread in the biological realm (Frölicher et al., 2016). It supports the selection of the most contrasting emission scenarios in regional downscaling of biological processes.

6) Projected increase in the EBS shelf summer bottom temperature is largely unchanged from CMIP5 RCP8.5 to CMIP6 SSP585 scenarios but large across-model spread persists from CMIP5 to CMIP6 projections; similarly, projected annual mean phytoplankton and large zooplankton biomass decreasing trends are comparable between RCP8.5 and SSP585 projections (Fig. 15). These results suggest that the projected long-term trend in EBS bottom temperature and plankton biomasses are robust responses to climate forcing.

Declaration of competing interest

The authors declare that they have no known competing financial interests or personal relationships that could have appeared to influence the work reported in this paper.

Appendix A. Supplementary data

Supplementary data to this article can be found online at https://doi.org/10.1016/j.dsr2.2021.104975.

References

Arrigo, K.R., Dijken, G. van, Pabi, S., 2008. Impact of a shrinking Arctic ice cover on marine primary production. Geophys. Res. Lett. 35 https://doi.org/10.1029/2008GL035028.

Aydin, K., Mueter, F., 2007. The Bering Sea—A dynamic food web perspective. Deep Sea Res. Part II Top. Stud. Oceanogr. 54, 2501–2525. https://doi.org/10.1016/j.dsr2.2007.08.022.

Bopp, L., Resplandy, L., Orr, J.C., Doney, S.C., Dunne, J.P., Gehlen, M., et al., 2013. Multiple stressors of ocean ecosystems in the 21st century: projections with CMIP5 models. Biogeosciences 10, 6225–6245. https://doi.org/10.5194/bg-10-6225-2013.

Brown, Z.W., Dijken, G.L. van, Arrigo, K.R., 2011. A reassessment of primary production and environmental change in the Bering Sea. J. Geophys. Res. Oceans 116. https://doi.org/10.1029/2010JC006766.

Bryndum-Buchholz, A., Tittensor, D.P., Blanchard, J.L., Cheung, W.W.L., Coll, M., Galbraith, E.D., et al., 2019. Twenty-first-century climate change impacts on marine animal biomass and ecosystem structure across ocean basins. Global Change Biol. 25, 459–472. https://doi.org/10.1111/gcb.14512.

Budgell, W.P., 2005. Numerical simulation of ice-ocean variability in the Barents Sea region. Ocean Dyn 55, 370–387. https://doi.org/10.1007/s10236-005-0008-3.

Cheng, W., Curchitser, E., Ladd, C., Stabeno, P., Wang, M., 2014. Influences of sea ice on the Eastern Bering Sea: NCAR CESM simulations and comparison with observations. Deep Sea Res. Part II Top. Stud. Oceanogr. 109, 27–38. https://doi.org/10.1016/j.dsr2.2014.03.002.

Cheng, W., Curchitser, E., Stock, C., Hermann, A., Cokelet, E., Mordy, C., et al., 2016. What processes contribute to the spring and fall bloom co-variability on the Eastern Bering Sea shelf? Deep Sea Res. Part II Top. Stud. Oceanogr. 134, 128–140. https://doi.org/10.1016/j.dsr2.2015.07.009.

Cheung, W.W.L., Bruggeman, J., Butenschön, M., 2019. Projected Changes in Global and National Potential Marine Fisheries Catch under Climate Change Scenarios in the Twenty-First Century. In: Bahri, M.T., Beveridge, M.C.M., Cochrane, K., Funge-Smith, S., Poulain, F. (Eds.), Food and Agriculture Organization of the United Nations, vol. 627, pp. 63–85. Rome, Italy, Impacts of Climate Change on Fisheries and Aquaculture: Synthesis of Current Knowledge, Adaptation and Mitigation Options Barange.

Coachman, L.K., 1986. Circulation, water masses, and fluxes on the southeastern Bering Sea shelf. Continent. Shelf Res. 5, 23–108.

Cullen, J.J., 2015. Subsurface chlorophyll maximum layers: enduring enigma or mystery solved? Ann. Rev. Mar. Sci. 71, 207–239.

Danabasoglu, G., Lamarque, J.-F., Bacmeister, J., Bailey, D.A., DuVivier, A.K., Edwards, J., et al., 2020. The community Earth system model Version 2 (CESM2). J. Adv. Model. Earth Syst. 12, e2019MS001916 https://doi.org/10.1029/2019MS001916.

Doney, S.C., 2006. Plankton in a warmer world. Nature 444, 695–696.

Drenkard, E., co-authors, 2021. Next-generation regional ocean projections for living marine resource management in a changing climate. ICES J. Mar. Sci. in press.

Dunne, J.P., Horowitz, L.W., Adcroft, A.J., Ginoux, P., Held, I.M., John, J.G., et al., 2020. The GFDL Earth system model Version 4.1 (GFDL-ESM 4.1): overall coupled model description and simulation characteristics. J. Adv. Model. Earth Syst. 12, e2019MS002015 https://doi.org/10.1029/2019MS002015.

Duffy-Anderson, J.T., Barbeaux, S.J., Farley, E., Heintz, R., Horne, J.K., Parker-Stetter, S.L., et al., 2016. The critical first year of life of walleye pollock (Gadus chalcogrammus) in the eastern Bering Sea: implications for recruitment and future research. Deep Sea Res. Part II Top. Stud. Oceanogr. 134, 283–301. https://doi.org/10.1016/j.dsr2.2015.02.001.

Duffy-Anderson, J.T., Stabeno, P., Andrews, A.G., Cieciel, K., Deary, A., Farley, E., et al., 2019. Responses of the northern Bering Sea and southeastern Bering Sea pelagic ecosystems following record-breaking low Winter sea ice. Geophys. Res. Lett. 46, 9833–9842. https://doi.org/10.1029/2019GL083396.

Eisner, L.B., Zuenko, Y.I., Basyuk, E.O., Britt, L.L., Duffy-Anderson, J.T., Kotwicki, S., et al., 2020. Environmental impacts on walleye pollock (Gadus chalcogramma) distribution across the Bering Sea shelf. Deep Sea Res. Part II Top. Stud. Oceanogr. 181–182, 104881 https://doi.org/10.1016/j.dsr2.2020.104881.

Eyring, V., Bony, S., Meehl, G.A., Senior, C.A., Stevens, B., Stouffer, R.J., Taylor, K.E., 2016. Overview of the coupled model intercomparison project phase 6 (CMIP6) experimental design and organization. Geosci. Model Dev. 9, 1937–1958. https://doi.org/10.5194/gmd-9-1937-2016.

Fairall, C., Bradley, E.F., Rogers, D.P., Edson, J.B., Young, G.S., 1996. Bulk parameterization of air-sea fluxes for Tropical Ocean-Global Atmosphere Coupled-Ocean Atmosphere Response Experiment. J. Geophys. Res. 101, 3747–3767. https://doi.org/10.1029/95JC03205.

Frölicher, T.L., Rodgers, K.B., Stock, C.A., Cheung, W.W.L., 2016. Sources of uncertainties in 21st century projections of potential ocean ecosystem stressors. Global Biogeochem. Cycles 30, 1224–1243. https://doi.org/10.1002/2015GB005338.

Gregory, J.M., Ingram, W.J., Palmer, M.A., Jones, G.S., Stott, P.A., Thorpe, R.B., et al., 2004. A new method for diagnosing radiative forcing and climate sensitivity. Geophys. Res. Lett. 31 https://doi.org/10.1029/2003GL018747.

Groeneveld, R.A., Bosello, F., Butenschön, M., Elliott, M., Peck, M.A., Pinnegar, J.K., 2018. Defining scenarios of future vectors of change in marine life and associated economic sectors. Estuar. Coast Shelf Sci. 201, 164–171. https://doi.org/10.1016/j.ecss.2015.10.020.

Gibson, G.A., Spitz, Y.H., 2011. Impacts of biological parameterisation, initial conditions, and environmental forcing on parameter sensitivity and uncertainty in a marine ecosystem model for the Bering Sea. J. Mar. Syst. 88, 214–231.

Gibson, G., Weijer, W., Jeffery, N., Wang, S., 2020. Relative impact of sea ice and temperature changes on arctic marine production. J. Geophys. Res. Biogeosci. 125, e2019JG005343 https://doi.org/10.1029/2019JG005343.

Haidvogel, D.B., Arango, H., Budgell, W.P., Cornuelle, B.D., Curchitser, E., Di Lorenzo, E., Fennel, K., Geyer, W.R., Hermann, A.J., Lanerolle, L., Levin, J., McWilliams, J.C., Miller, A.J., Moore, A.M., Powell, T.M., Shchepetkin, A.F., Sherwood, C.R., Signell, R.P., Warner, J.C., Wilkin, J., 2008. Regional ocean forecasting in terrain- following coordinates: model formulation and skill assessment. J. Comput. Phys. 227, 3595–3624.

Hajima, T., Watanabe, M., Yamamoto, A., Tatebe, H., Noguchi, M.A., Abe, M., et al., 2020. Development of the MIROC-ES2L Earth system model and the evaluation of biogeochemical processes and feedbacks. Geosci. Model Dev. 13, 2197–2244. https://doi.org/10.5194/gmd-13-2197-2020.

Hawkins, E., Sutton, R., 2009. The potential to narrow uncertainty in regional climate predictions. Bull. Am. Meteorol. Soc. 90, 1095–1108.

Henson, S., Cole, H., Beaulieu, C., Yool, A., 2013. The impact of global warming on seasonality of ocean primary production. Biogeosciences 10, 4357–4369.

Hermann, A.J., Gibson, G.A., Bond, N.A., Curchitser, E.N., Hedstrom, K., Cheng, W., et al., 2013. A multivariate analysis of observed and modeled biophysical variability on the Bering Sea shelf: multidecadal hindcasts (1970–2009) and forecasts (2010–2040). Deep Sea Res. Part II Top. Stud. Oceanogr. 94, 121–139. https://doi.org/10.1016/j.dsr2.2013.04.007.

Hermann, A.J., Gibson, G.A., Bond, N.A., Curchitser, E.N., Hedstrom, K., Cheng, W., et al., 2016. Projected future biophysical states of the Bering Sea. Deep Sea Res. Part II Top. Stud. Oceanogr. 134, 30–47.

Hermann, A.J., Gibson, G.A., Cheng, W., Ortiz, I., Aydin, K., Wang, M., et al., 2019. Projected biophysical conditions of the Bering Sea to 2100 under multiple emission scenarios. ICES J. Mar. Sci. 76, 1280–1304.

Hermann, A.J., Kearney, K., Cheng, W., Pilcher, D., Aydin, K., Holsman, K.K., Hollowed, A.B., 2021. Coupled modes of projected regional change in the Bering Sea from a dynamically downscaling model under CMIP6 forcing. Deep Sea Res. Part II Top. Stud. Oceanogr. this issue.

Hollowed, A.B., Holsman, K.K., Haynie, A.C., Hermann, A.J., Punt, A.E., Aydin, K., et al., 2020. Integrated modeling to evaluate climate change impacts on coupled social-ecological systems in Alaska. Front. Mar. Sci. 6, 775.

Holsman, K.K., Haynie, A.C., Hollowed, A.B., Reum, J.C.P., Aydin, K., Hermann, A.J., et al., 2020. Ecosystem-based fisheries management forestalls climate-driven collapse. Nat. Commun. 11, 4579. https://doi.org/10.1038/s41467-020-18300-3.

Kay, J.E., Deser, C., Phillips, A., Mai, A., Hannay, C., Strand, G., et al., 2015. The Community Earth System Model (CESM) Large Ensemble Project: A Community Resource for Studying Climate Change in the Presence of Internal Climate Variability. Bull. Am. Meteorol. Soc. 96, 1333–1349. https://doi.org/10.1175/BAMS-D-13-00255.1.

Kearney, K.A., 2019. Freshwater input to the Bering Sea, 1950-2017. U.S. Dep. Commer., NOAA Tech. Memo. NMFS-AFSC-388, 46 p.

Kearney, K., Hermann, A., Cheng, W., Ortiz, I., Aydin, K., 2020. A coupled pelagic–benthic–sympagic biogeochemical model for the Bering Sea: documentation and validation of the BESTNPZ model (v2019. 08.23) within a high-resolution regional ocean model. Geosci. Model Dev. 13, 597–650.

Kwiatkowski, L., Torres, O., Bopp, L., Aumont, O., Chamberlain, M., Christian, J.R., Dunne, J.P., Gehlen, M., Ilyina, T., John, J.G., Lenton, A., Li, H., Lovenduski, N.S., Orr, J.C., Palmieri, J., Santana-Falcón, Y., Schwinger, J., Séférian, R., Stock, C.A., Tagliabue, A., Takano, Y., Tjiputra, J., Toyama, K., Tsujino, H., Watanabe, M., Yamamoto, A., Yool, A., Ziehn, T., 2020. Twenty-first century ocean warming, acidification, deoxygenation, and upper-ocean nutrient and primary production decline from CMIP6 model projections. Biogeosciences 17, 3439–3470. https://doi.org/10.5194/bg-17-3439-2020, 2020.

Lee, H.-C., Delworth, T.L., Rosati, A., Zhang, R., Anderson, W.G., Zeng, F., et al., 2013. Impact of climate warming on upper layer of the Bering Sea. Clim. Dynam. 40, 327–340. https://doi.org/10.1007/s00382-012-1301-8.

Marchesiello, P., McWilliams, J.C., Shchepetkin, A., 2001. Open boundary conditions for long-term integration of regional oceanic models. Ocean Model. 3, 1–20.

Martin, J., Tremblay, J.É., Price, N.M., 2012. Nutritive and photosynthetic ecology of subsurface chlorophyll maxima in Canadian Arctic waters. Biogeosciences 9, 5353–5371.

Mastrandrea, M.D., Mach, K.J., Plattner, G.-K., Edenhofer, O., Stocker, T.F., Field, C.B., et al., 2011. The IPCC AR5 guidance note on consistent treatment of uncertainties: a common approach across the working groups. Climatic Change 108, 675. https://doi.org/10.1007/s10584-011-0178-6.

O'Neill, B.C., Kriegler, E., Riahi, K., Ebi, K.L., Hallegatte, S., Carter, T.R., et al., 2014. A new scenario framework for climate change research: the concept of shared socioeconomic pathways. Climatic Change 122, 387–400. https://doi.org/10.1007/s10584-013-0905-2.

O'Neill, B.C., Tebaldi, C., van Vuuren, D.P., Eyring, V., Friedlingstein, P., Hurtt, G., et al., 2016. The scenario model intercomparison project (ScenarioMIP) for CMIP6. Geosci. Model Dev 9, 3461–3482. https://doi.org/10.5194/gmd-9-3461-2016.

Ortiz, I., Aydin, K., Hermann, A.J., Gibson, G.A., Punt, A.E., Wiese, F.K., et al., 2016. Climate to fish: synthesizing field work, data and models in a 39-year retrospective analysis of seasonal processes on the eastern Bering Sea shelf and slope. Deep Sea Res. Part II Top. Stud. Oceanogr. 134, 390–412.

Payne, M.R., Kudahl, M., Engelhard, G.H., Peck, M.A., Pinnegar, J.K., 2020. Climate risk to European fisheries and coastal communities. BioRxiv. https://doi.org/10.1101/2020.08.03.234401, 08.03.234401, 2020.

Pilcher, D.J., Naiman, D.M., Cross, J.N., Hermann, A.J., Siedlecki, S.A., Gibson, G.A., Mathis, J.T., 2019. Modeled effect of coastal biogeochemical processes, climate Variability, and ocean acidification on aragonite saturation state in the Bering Sea. Front. Mar. Sci. 5 https://doi.org/10.3389/fmars.2018.00508.

Pilcher, D.J., Cross, J.N., Hermann, A.J., Kearney, K., Cheng, W., Mathis, J., 2021. Dynamically downscaled projections of ocean acidification for the Bering Sea. Deep Sea Res. Part II Top. Stud. Oceanogr. this issue.

Reum, J.C., Blanchard, J.L., Holsman, K.K., Aydin, K., Hollowed, A.B., Hermann, A.J., et al., 2020. Ensemble projections of future climate change impacts on the Eastern Bering Sea food web using a multispecies size spectrum model. Front. Mar. Sci. 7, 124. https://doi.org/10.3389/fmars.2020.00124.

Séférian, R., Berthet, S., Yool, A., Palmiéri, J., Bopp, L., Tagliabue, A., et al., 2020. Tracking improvement in simulated marine biogeochemistry between CMIP5 and CMIP6. Curr. Clim. Change Rep. 6, 95–119. https://doi.org/10.1007/s40641-020-00160-0.

Siddon, E., 2020. Ecosystem Status Report for the Eastern Bering Sea. In: Stock Assessment and Fishery Evaluation Report, vol. 1007. North Pacific Fishery Management Council. West Third, Suite 400, Anchorage, AK 99501.

Sigler, M.F., Harvey, H.R., Ashjian, J., Lomas, M.W., Napp, J.M., Stabeno, P.J., Van Pelt, T.I., 2010. How does climate change affect the Bering Sea ecosystem? Eos. Trans. Am. Geophys. Union 91, 457–458. https://doi.org/10.1029/2010EO480001.

Sigler, M.F., Stabeno, P.J., Eisner, L.B., Napp, J.M., Mueter, F.J., 2014. Spring and fall phytoplankton blooms in a productive subarctic ecosystem, the eastern Bering Sea,

during 1995–2011. Deep Sea Res. Part II Top. Stud. Oceanogr. 109, 71–83. https://doi.org/10.1016/j.dsr2.2013.12.007.

Stabeno, P.J., Reed, R.K., Napp, J.M., 2002. Transport through Unimak pass, Alaska. Deep Sea Res. Part II Top. Stud. Oceanogr. 49, 5919–5930. https://doi.org/10.1016/S0967-0645(02)00326-0.

Stabeno, P.J., Farley, E., Kachel, N., Moore, S., Mordy, C., Napp, J.M., Overland, J.E., Pinchuk, A.I., Sigler, M., 2012. A comparison of the physics of the northern and southern shelves of the eastern Bering Sea and some implications for the ecosystem. Deep Sea Res. Part II Top. Stud. Oceanogr. 65–70, 14–30.

Stabeno, P.J., Duffy-Anderson, J.T., Eisner, L.B., Farley, E.V., Heintz, R.A., Mordy, C.W., 2017. Return of warm conditions in the southeastern Bering Sea: physics to fluorescence. PLOS ONE 12, e0185464. https://doi.org/10.1371/journal.pone.0185464.

Stabeno, P.J., Bell, S.W., 2019. Extreme conditions in the Bering Sea (2017–2018): record-breaking low Sea-Ice extent. Geophys. Res. Lett. 46, 8952–8959. https://doi.org/10.1029/2019gl083816.

Stevenson, D.E., Lauth, R.R., 2019. Bottom trawl surveys in the northern Bering Sea indicate recent shifts in the distribution of marine species. Polar Biol. 42, 407–421. https://doi.org/10.1007/s00300-018-2431-1.

Stock, C.A., Dunne, J.P., Fan, S., Ginoux, P., John, J., Krasting, J.P., et al., 2020. Ocean Biogeochemistry in GFDL's Earth system model 4.1 and its response to increasing atmospheric CO_2. J. Adv. Model. Earth Syst. 12, e2019MS002043 https://doi.org/10.1029/2019MS002043.

Strom, S.L., Fredrickson, K.A., 2008. Intense stratification leads to phytoplankton nutrient limitation and reduced microzooplankton grazing in the southeastern Bering Sea. Deep Sea Res. Part II Top. Stud. Oceanogr. 55, 1761–1774. https://doi.org/10.1016/j.dsr2.2008.04.008.

Tittensor, D.P., Eddy, T.D., Lotze, H.K., Galbraith, E.D., Cheung, W., Barange, M., et al., 2018. A protocol for the intercomparison of marine fishery and ecosystem models: fish-MIP v1.0. Geosci. Model Dev 11, 1421–1442. https://doi.org/10.5194/gmd-11-1421-2018.

Watanabe, S., Hajima, T., Sudo, K., Nagashima, T., Takemura, T., Okajima, H., et al., 2011. MIROC-ESM 2010: model description and basic results of CMIP5-20c3m experiments. Geosci. Model Dev. 4, 845–872. https://doi.org/10.5194/gmd-4-845-2011.

Zelinka, M.D., Myers, T.A., McCoy, D.T., Po-Chedley, S., Caldwell, P.M., Ceppi, P., et al., 2020. Causes of higher climate sensitivity in CMIP6 models. Geophys. Res. Lett. 47, e2019GL085782 https://doi.org/10.1029/2019GL085782.